

University of New Hampshire
University of New Hampshire Scholars' Repository

Master's Theses and Capstones

Student Scholarship

Spring 2008

An autonomous orbit transfer controller for the NASA Magnetospheric MultiScale satellite

Michael Borrelli

University of New Hampshire, Durham

Follow this and additional works at: <https://scholars.unh.edu/thesis>

Recommended Citation

Borrelli, Michael, "An autonomous orbit transfer controller for the NASA Magnetospheric MultiScale satellite" (2008). *Master's Theses and Capstones*. 354.

<https://scholars.unh.edu/thesis/354>

This Thesis is brought to you for free and open access by the Student Scholarship at University of New Hampshire Scholars' Repository. It has been accepted for inclusion in Master's Theses and Capstones by an authorized administrator of University of New Hampshire Scholars' Repository. For more information, please contact nicole.hentz@unh.edu.

AN AUTONOMOUS ORBIT TRANSFER CONTROLLER FOR THE NASA
MAGNETOSPHERIC MULTISCALE SATELLITE

BY

MICHAEL BORRELLI

B.S., University of New Hampshire, 2006

THESIS

Submitted to the University of New Hampshire

in Partial Fulfillment of

the Requirement for the Degree of

Master of Science

in

Mechanical Engineering

May, 2008

UMI Number: 1454986

INFORMATION TO USERS

The quality of this reproduction is dependent upon the quality of the copy submitted. Broken or indistinct print, colored or poor quality illustrations and photographs, print bleed-through, substandard margins, and improper alignment can adversely affect reproduction.

In the unlikely event that the author did not send a complete manuscript and there are missing pages, these will be noted. Also, if unauthorized copyright material had to be removed, a note will indicate the deletion.

UMI[®]

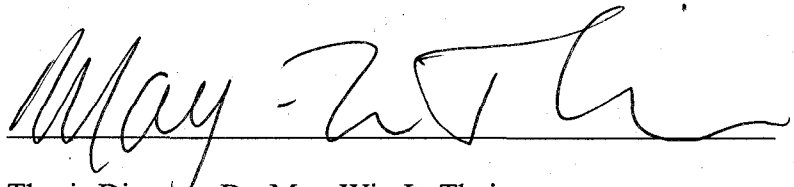
UMI Microform 1454986

Copyright 2008 by ProQuest LLC.

All rights reserved. This microform edition is protected against unauthorized copying under Title 17, United States Code.

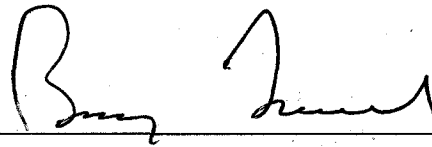
ProQuest LLC
789 E. Eisenhower Parkway
PO Box 1346
Ann Arbor, MI 48106-1346

This thesis has been examined and approved.



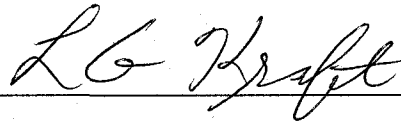
Thesis Director, Dr. May-Win L. Thein

Associate Professor of Mechanical Engineering



Dr. Barry Fussel

Professor of Mechanical Engineering



Dr. L. Gordon Kraft, III

Professor of Electrical and Computer Engineering

5/13/08

Date

ACKNOWLEDGEMENTS

The author would like to acknowledge the invaluable assistance of the engineers at NASA Goddard Space Flight Center, especially Josephine K. San and Dean C. Tsai, as well as the New Hampshire NASA Space Grant Consortium, without all of whom this work would not have been possible.

TABLE OF CONTENTS

ACKNOWLEDGEMENTS	iii
LIST OF TABLES	vii
LIST OF FIGURES	viii
ABSTRACT	xi

<u>CHAPTER</u>	<u>PAGE</u>
1. INTRODUCTION	1
1.1 NASA Magnetospheric MultiScale Mission	1
1.2 Research Objectives.....	2
1.3 Past Research	3
1.4 Thesis Contribution.....	4
1.5 Thesis Outline	5
2. SPACE ENVIRONMENT AND REFERENCE FRAMES	6
2.1 Orbital Elements and Transfers	6
2.1.1 Semi-Major Axis Criterion	9
2.2 Coordinate Systems	9
2.2.1 Spacecraft Inertial (SCI) Coordinates.....	10
2.2.2 Spacecraft-Fixed (SCF) Coordinates.....	11
2.2.3 Orbit Defined Coordinate Systems (OCS).....	11
2.3 Coordinate Transformations	11

2.3.1	Euler Angle Transformations.....	12
2.4	Orbital Control Overview	13
3.	FLIGHT HARDWARE	15
3.1	Accelerometers	15
3.2	Star Trackers	16
3.3	Thrusters	16
4.	SYSTEM DESIGN	18
4.1	Satellite Model and Inputs	18
4.2	Thruster Model.....	20
4.3	Coordinate Transformations	20
4.4	Controller Design.....	22
4.4.1	PID Gain Selection	22
4.4.2	Radial Thruster Timing.....	25
4.4.3	Axial Thruster Timing	26
4.4.4	Shutoff Criteria	27
4.4.5	Hysteresis Relays.....	28
4.5	Sensor and Noise Models.....	29
4.6	Relevant Disturbances	31
4.6.1	Nutation.....	31
4.6.2	Thruster Bias and Misalignments	33
4.6.3	Sine Component of Radial Thrust.....	33
5.	RESULTS	35
5.1	Study One: Ideal Case.....	36

5.2 Study Two: Misalignments Only	41
5.3 Study Three: Nutation Only	44
5.4 Study Four: Thruster Bias Only	49
5.5 Study Five: Nutation, Misalignments and Thruster Bias	52
5.6 Sensitivity to Orientation	54
5.7 Use of Semi-Major Axis Shutoff vs. Delta-V Shutoff	59
5.8 Effect of Accelerometer Bias on Errors	61
6. CONCLUSIONS AND FUTURE WORK	63
6.1 Research Summary	63
6.2 Future Work	65
BIBLIOGRAPHY	67
APPENDICES	68
A MATLAB FILE	69
B SIMULINK BLOCK DIAGRAMS	77
C SEMI-MAJOR AXIS SENSITIVITY DERIVATION	83

LIST OF TABLES

2.1: Keplerian Orbital Elements	6
4.1: PID gain matrices.....	24
5.1: Results from the ideal case	37
5.2: Results from misalignment case	42
5.3: Results from the nutation study, no relays.....	45
5.4: Results from the nutation case using relays.....	47
5.5: Results from the thruster bias case	50
5.6: Results for a worst case scenario	53
5.7: Overall results from axial tilt test for $\varphi = 0^\circ$ and $\varphi = 180^\circ$	59
5.8: Resulting errors and efficiencies when using an SMA shutoff of ± 50 meters	60
5.9: Resulting errors and efficiencies when using a ΔV shutoff of $\pm 1\%$	60
5.10: Resulting errors and efficiencies when using no controller shutoffs.....	61
5.11: Effect of accelerometer bias levels on the SMA and ΔV errors.....	62

LIST OF FIGURES

1-1: Three major orbital transfers from the mission design of the MMS constellation.....	2
2-1: Graphical representation of an orbit's Keplerian elements.....	7
2-2: Earth- and Spacecraft-Centered Systems	10
2-3: Radial thrust visualization, depicting starting and stopping points of the radial thruster	13
2-4: Radial burn angle window 2β as seen from inertial frame perspective.....	14
4-1: Simulink thruster model	20
4-2: Result from sending smooth control signals into the actuator model	22
4-3: Simple representation of the main system dynamics and simulation blocks	24
4-4: Tangent of firing window β provides timing algorithm for radial burns	26
4-5: Depiction of relay with hysteresis	28
4-6: Dean Tsai's accelerometer noise model, using three frequency ranges and Butterworth filters.....	29
4-7: Power Density Spectrum from the "true" accelerometer noise model	30
4-8: Comparison of PSD plots from "true" and simplified noise models.....	31
4-9: Nutation angle requirement θ_n	32
4-10: Sine and cosine components of radial thrust for a given θ_e	34
5-1: Position error, velocity error, ΔV used and major results for the ideal case	37
5-2: SMA error for the ideal case	38

5-3: Radial and axial thrust profile for the ideal case	39
5-4: Close-up of radial thrust profile	40
5-5: Position errors, velocity errors and ΔV used for the misalignment case.....	42
5-6: SMA error for the misalignment case	43
5-7: Radial and axial thrust profiles for the misalignment case.....	44
5-8: Position errors, velocity errors and ΔV used from the nutation case, no relays inc..	45
5-9: Thrust profile for the nutation case, no relays included	46
5-10: Position error, velocity error and ΔV used for the nutation case using relays	47
5-11: SMA error for the nutation case with relays	48
5-12: Thrust profile for the nutation case with relays.....	49
5-13: Position error, velocity error and ΔV used for the thruster bias case.....	50
5-14: SMA error for the thruster bias case.....	51
5-15: Thrust profile for the thruster bias case.....	51
5-16: Position error, velocity error and V used for a worst case scenario	52
5-17: SMA error for a worst case scenario	53
5-18: Thrust profile for a worst case scenario	54
5-19: Three-dimensional visual results from the tilt test, depicting all 100 unique axial tilts with respect to the fixed inertial frame (dotted lines).....	56
5-20: Top-down image of results from the tilt test, $\varphi = 0^\circ$	56
5-21: Number of occurrences of ΔV error ranges, $\varphi = 0^\circ$	57
5-22: Top-down image of results from the tilt test, $\varphi = 180^\circ$	58
5-23: Number of occurrences of ΔV error ranges, $\varphi = 180^\circ$	58

B-1: Main system in Orbit1.mdl	77
B-2: True satellite model, including accelerometer model, gravitational acceleration and plant dynamics	78
B-3: Target satellite model, including gravitational acceleration, which outputs position and velocity vectors to generate and error vector	78
B-4: Direction Cosine Matrix generator, including Euler Rate subsystem	79
B-5: Euler angel rate calculation based upon body rate inputs and Euler angle initial conditions.....	79
B-6: Controller subsystem, including radial thruster timing algorithm and radial burn angle window reducing algorithm, as well as the thruster model.....	80
B-7: Thruster model subsystem, including axial pause and relays, as well as the thruster misalignment/bias subsystem.....	80
B-8: Final thruster calculations, including sine/cosine components of radial force and the efficiency calculation and Delta-V subsystem.....	81
B-9: Delta-V subsystem.....	81

ABSTRACT

AN AUTONOMOUS ORBIT TRANSFER CONTROLLER FOR THE NASA

MAGNETOSPHERIC MULTISCALE SATELLITE

by

Michael Borrelli

University of New Hampshire, May, 2008

With the ever more demanding goals of space exploration and research comes the need for more complex mission planning. Part of this complexity manifests itself in a satellite's orbit specifications. An increasing number of explorer missions call for a group of satellites to maneuver while arranged in a tightly controlled formation, or constellation. In order to maintain these constellations at immense distances from Earth, engineers must rely on feedback systems within the satellites' hardware. Controllers are created to manipulate the actuators, such as thrusters, and are therefore responsible for the economical use of fuel; overusing fuel can reduce a satellite's useful lifetime. It is necessary to achieve all controller demands while monitoring fuel consumption when developing a system such as the one presented by this thesis.

This thesis presents a detailed method of obtaining a simplified model of a spin-stabilized spacecraft and its environment, including relevant uncertainties, disturbances and sensor models. This thesis shows through rigorous simulations that it is feasible to control orbit maneuvers of spin-stabilized spacecraft to very strict specifications, despite the inclusion of sensor noise, thruster disturbance and bias, and nutation effects.

CHAPTER 1

INTRODUCTION

1.1 NASA Magnetospheric MultiScale Mission

Recent work at NASA Goddard Space Flight Center (GSFC) has included detailed analyses for the Magnetospheric MultiScale (MMS) mission. It is the goal of the MMS mission to more fully characterize, both spatially and temporally, the fluctuations that occur in the process known as magnetic reconnection. Earth, like any iron core, has magnetic field lines emanating from its center which stretch out many thousands of miles into space. These magnetic field lines are a boon to the inhabitants of the planet, as they offer a protection from highly energetic particles which travel at immense velocities through space in the form of solar wind. The field lines are deflected due to this energetic collision and bent around Earth into a long, stretched portion. Here, the field lines reconnect into a section known as the magnetotail. It is in this section that the spacecraft will perform the majority of the scientific measurements.

The MMS mission, planned to launch in 2014, will consist of a group of four satellites which will maintain a tetrahedron formation (the “constellation”) through high-altitude and highly elliptic orbits. There will be several large orbital maneuvers in the early stages of the mission (see Figure 1-1), as is normally the case in high-altitude orbit missions [7], and these maneuvers can typically induce unwanted motion and rotation in the spacecraft. To overcome this problematic possibility, the four MMS spacecraft will

maintain a rotation about their body-z axes so that they are spin-stabilized (stabilized by a fixed angular momentum vector). Spin-stabilized craft are less susceptible to torque disturbances [4]. However, with the benefit of stabilization comes the difficult task of orbital maneuvering. Since the satellite is spinning on its body z-axis, any thrusts performed in the radial direction (i.e. perpendicular to the axis of rotation) must be aligned with an error vector, else the thrusts will propel the spacecraft in an unintended direction.

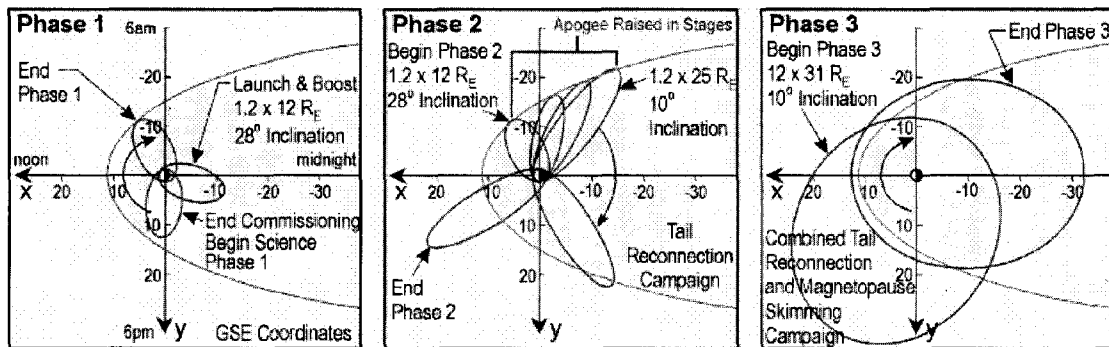


Figure 1-1: Three major orbital transfers from the mission design of the MMS constellation

1.2 Research Objectives

The work described in this thesis is an ongoing collaboration with NASA GSFC, located in Greenbelt, Maryland. This work is a parallel study that is performed with very limited knowledge of the standard procedures by which NASA facilities will typically operate. It is the goal of the engineers at GSFC's Flight Dynamics Analysis Branch that, while using inherently different approaches, the results of this thesis confirm and support their own independent conclusions.

The objective of this research is to ascertain the feasibility of using an on-board, closed-loop orbital maneuver controller on a small spin-stabilized satellite. To date, no such control for this type of spacecraft mission has been developed. In order to do this, there is also an inherent requirement of obtaining a conservative, yet accurate, model of the satellite environment, including any perturbations that the spacecraft may encounter. The system must also take into account any coordinate transformations necessary to perform orbital maneuvers. Although the MMS mission consists of four satellites in a constellation, it is beyond the scope of this thesis to determine the effectiveness of this controller in maintaining that constellation. Instead, requirements for “successful” control are measured by the ability of the control system to limit the error for one spacecraft in orbit semi-major axis to less than 50 meters, the error in the velocity change (ΔV) to less than 1%, and finally to limit the ratio of projected ΔV to expended ΔV so it does not fall below 90%. This thesis also seeks to develop this orbital controller without any loss of generality, so that these results can be applied to any MMS system without compromising the validity.

1.3 Past Research

Much work has been done in the area of feedback control aboard spacecraft. However, the vast majority of this research has focused on either attitude control or orbit maintenance, also known as “station-keeping.” Koprubasi [2] examines the use of nonlinear feedback methods in obtaining accurate attitude estimates, and Mushaweh [1] uses linear and nonlinear methods for attitude estimation, attitude control, and nutation control. Mushaweh’s work is also with particular reference to the NASA MMS mission. However, the limited capabilities of the thruster actuators aboard the MMS spacecraft are

neglected and thrust is assumed to be available in proportion to the feedback errors. Clemente [3] again performs research specific to the MMS mission; his work is an optimization study to compare actively controlled satellite formations to passively controlled formations. His results suggest that actively controlled formations are optimal in terms of formation drift. Again, however, force is assumed available in all directions and at all times, thus neglecting the spinning behavior of the spacecraft.

1.4 Thesis Contribution

This research contributes to the field of feedback control, particularly in relation to spacecraft orbit planning, in the following ways:

- Creation of a simplified, yet accurate model of a spin-stabilized spacecraft and its environment
- Application of a closed-loop control system with respect to orbit maneuvers for a body with two degrees of freedom
- Creation of a timing algorithm for radial thrusters that spin with the spacecraft body
- Inclusion of common orbit disturbances, such as nutation and actuator misalignments, to measure the robustness of the orbital control system
- Quantitative and qualitative results describing the capabilities of a common linear controller for this application

1.5 Thesis Outline

The remaining chapters are organized as follows:

- Chapter 2, Space Environment and Reference Frames – This chapter details the necessary considerations in establishing an accurate orbital environment. Keplerian Orbital Elements are introduced, as well as common reference frames used in orbit planning. Coordinate transformations are briefly described.
- Chapter 3, Flight Hardware – This chapter briefly describes the sensors and actuators that are expected to be implemented aboard the MMS spacecraft.
- Chapter 4, System Design – This chapter details all the considerations that are taken into account while designing this system in MATLAB/Simulink, such as the satellite and actuator models, coordinate transformations, disturbance models, and controller design.
- Chapter 5, Results – The results are presented and discussed. Testing is performed by way of several case studies, in which the controller is tested against disturbances, orientation and sensor biases.
- Chapter 6, Conclusions and Future Work – This chapter presents the conclusions that are drawn from all available results and the recommendations for any future work that aims towards fully characterizing this controller.

CHAPTER 2

SPACE ENVIRONMENT AND REFERENCE FRAMES

2.1 Orbital Elements and Transfers

Analogous to a position and velocity described in a Cartesian coordinate system, an object in an elliptical orbit can be described using six parameters, collectively known as the object's *ephemeris*. Logsdon [6] describes these parameters, or Keplerian Orbital Elements, as shown in Table 2.1 and Wei [8] depicts them graphically in Figure 2-1:

Element	Symbol	Description	Unit of Meas.
Semi-Major Axis	a	The half-length of the ellipse	[km], [mi]
Orbital Inclination	i	The angle between the orbital plane and the equatorial plane	[rad], [deg]
Argument of Perigee	ω	The location of the perigee point	[rad],[deg]
Orbital Eccentricity	e	The 'oblateness' of the orbit	$0 < e < 1$
Ascending Node	Ω	The longitude of the ascending node (equatorial crossing)	[rad],[deg]
Time of Perigee Passage	T	The time of passage of the point of closest approach to the Earth	[sec],[hr]

Table 2.1: Keplerian Orbital Elements

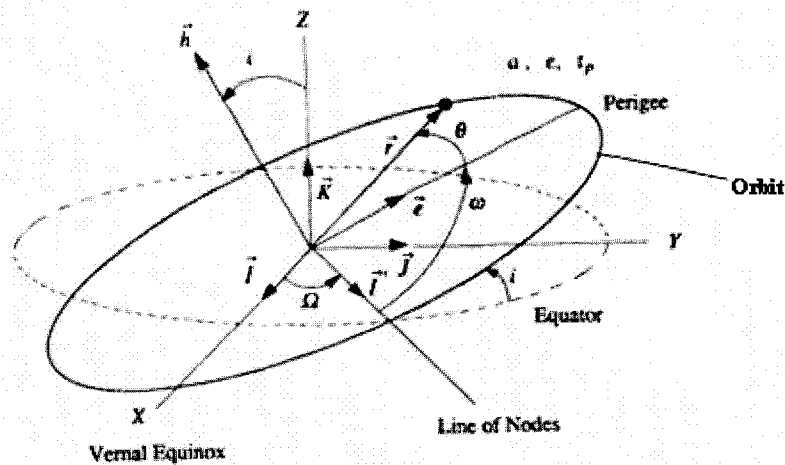


Figure 2-1: Graphical representation of an orbit's Keplerian elements

In any elliptical orbit, there are two points that determine the overall size and shape (oblateness) of the orbit: the distance to apogee, r_a , and the distance to perigee, r_p , both with respect to the orbital center. The apogee denotes the farthest point of the orbit from Earth while the perigee denotes the closest. Of the six elements, two are functions of r_a and r_p : the semi-major axis *SMA* and the eccentricity e , respectively by the following equations:

$$SMA = \frac{1}{2}(r_a + r_p) \quad (2.1)$$

$$e = \frac{r_a - r_p}{r_a + r_p} \quad (2.2)$$

Of the remaining four elements, three describe the orientation of the orbit with respect to the fixed coordinate frame of Earth: the orbital inclination, the argument of perigee, and the ascending node. The final element—the time of perigee passage—is an initial condition that allows for the calculation of a body's exact position along the orbital trajectory at any given time. For the purposes of this research, this element is substituted

for the actual position of the satellite along the trajectory, known as the true anomaly ν , which is measured in degrees or radians.

It is possible to convert between the six orbital elements and the more useful (in a controls sense) position and velocity vectors. From [5], the equations for the position vector are:

$$x = r \cdot [\cos(\omega + \nu) \cos \Omega - \cos i \cdot \sin(\omega + \nu) \sin \Omega] \quad (2.3a)$$

$$y = r \cdot [\cos(\omega + \nu) \sin \Omega + \cos i \cdot \sin(\omega + \nu) \cos \Omega] \quad (2.3b)$$

$$z = r \cdot [\sin(\omega + \nu) \sin i] \quad (2.3c)$$

The equations for the velocity vector are:

$$\dot{x} = \sqrt{\frac{\mu}{P}} \cdot [(\cos \nu + e)(-\sin \omega \cdot \cos \Omega - \cos i \cdot \sin \Omega \cdot \cos \omega) - \sin \nu (\cos \omega \cdot \cos \Omega - \cos i \cdot \sin \omega \cdot \sin \Omega)] \quad (2.4a)$$

$$\dot{y} = \sqrt{\frac{\mu}{P}} \cdot [(\cos \nu + e)(-\sin \omega \cdot \sin \Omega + \cos i \cdot \cos \omega) - \sin \nu (\cos \omega \cdot \sin \Omega + \cos i \cdot \sin \omega \cdot \cos \Omega)] \quad (2.4b)$$

$$\dot{z} = \sqrt{\frac{\mu}{P}} \cdot [(\cos \nu + e) \sin i \cdot \cos \omega - \sin \nu \cdot \sin i \cdot \sin \omega] \quad (2.4c)$$

where $\mu = 3.986 \cdot 10^8 \text{ m}^3 / \text{s}^2$ is the gravitational constant of Earth, $P[\text{meters}] = a \cdot (1 - e^2)$ is the semilatus rectum, otherwise known as the “parameter”, and $r[\text{meters}] = P(1 + e \cos \nu)^{-1}$ is the radial distance with respect to the orbital center (one of the elliptical foci). The parameter is a distance measurement that describes the length of the axis that runs through the focus of the ellipse and is also perpendicular to the semi-major axis. It can be seen that when $\nu = \pm\pi/2$, $r = P$.

2.1.1 Semi-Major Axis Criterion

The semi-major axis of the orbit is one of the primary values considered in the objectives. From [5] it is seen that the velocity magnitude can be calculated from the energy balance equation:

$$v^2 = \frac{2\mu}{r} - \frac{\mu}{SMA} \quad (2.5)$$

This equation can be rearranged to solve for the semi-major axis a such that:

$$SMA = \frac{r}{2 - \left(\frac{v^2 r}{\mu}\right)} \quad (2.5a)$$

In a derivation (see Appendix C) where the derivative of SMA is taken with respect to both r and v , it is found that for a given pair of ΔV and Δr , the maximum deviation in semi-major axis is:

$$\Delta SMA = (6.157 \times 10^{-1}) \Delta r + (9.115 \times 10^3) \Delta v \quad (2.6)$$

This derivation shows that the change in SMA is far more sensitive to velocity changes than to position changes. Note that although this derivation takes only the velocity and position changes along the orbit trajectory into account (i.e. no out-of-plane changes), it is a clear indicator of the necessary weighting in terms of the importance of errors.

2.2 Coordinate Systems

When planning and modeling a satellite mission, it is crucial to establish which coordinate systems are being referenced at any point in time. There is a reference frame which describe ground-based measurements, known as the Earth-centered inertial (ECI)

reference frame, as well as frames which describe measurements relative to the spacecraft, known as body-centered frames. For a more detailed description of coordinate frames, the reader is referred to [4], [5] and [7]. Figure 2-2 depicts the various coordinate frames (adapted from [2]). Three different types of body-centered frames are discussed here.

2.2.1 Spacecraft Inertial (SCI) Coordinates

Spacecraft centered inertial frames are commonly used in mission planning and spacecraft motion. This coordinate frame translates with the spacecraft but its axes are aligned with the Earth inertial axes and do not rotate with the spacecraft. As such, no coordinate transformations are required when relating measurements between ground stations and the spacecraft. This reference frame is used in preliminary simulations before considering the spinning and nutation of the satellites and the possibility of body reorientation.

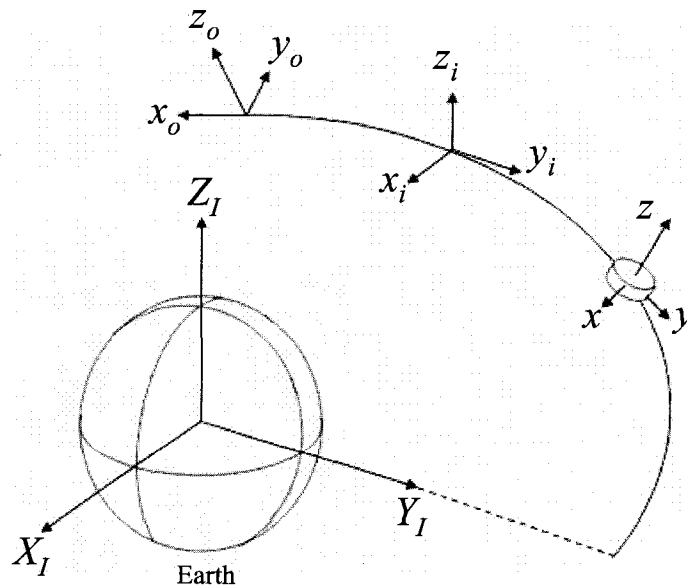


Figure 2-2: Earth- and Spacecraft-Centered Systems

2.2.2 Spacecraft-Fixed (SCF) Coordinates

Spacecraft-centered, fixed frames have axes which are usually fixed along the inertial axes of the craft. These frames both translate and rotate with the spacecraft, making fixed frames ideal for attitude measurements and control purposes. The SCF frame is the primary spacecraft reference frame used in this research.

2.2.3 Orbit Defined Coordinate Systems (OCS)

Orbit defined coordinate systems translate with the spacecraft but have axes that are dependent on the orbital trajectory itself. Typically, one axis (usually the x-axis) is collinear with the instantaneous orbit trajectory (referred to as the *in-track* direction) while another axis is normal to the plane of the orbit. The third axis completes the orthogonal triad (referred to as the *cross-track* direction). For this research, an OCS is used when referencing velocity inputs to the system; a ΔV vector of $[1 \ 1 \ 1]^T$ m/s would indicate 1m/s in each of the in-track, cross-track and orbit-normal directions.

2.3 Coordinate Transformations

In order to represent Earth-referenced measurements and vectors in the spacecraft fixed frame, it is necessary to perform coordinate transformations. There are different methods of representing the rotations required to transform a vector from one frame to another. The one used in this research is the common Euler angle representation; however in many space science applications, it is typical to use quaternion rotations. Presented here is a brief overview of the Euler angle transformation. For more detail of Euler angles, the reader is referred to [4] and [5].

2.3.1 Euler Angle Transformations

It is possible to represent any rotation of a body frame from a reference frame as a set of at most three pure angle rotations (i.e. yaw, pitch, and roll). These rotations are called Euler angles and are referred to as ψ , θ , and ϕ . A common sequence of rotations is the 3-1-3 transformation, which refers to rotation about the body z-axis, followed by a rotation about the body x-axis, and finally a second rotation about the body z-axis. This sequence is used throughout this research. Each rotation sequence has a unique 3x3 rotation matrix, referred to as the *Direction Cosine Matrix* denoted by $\alpha \in \mathcal{R}^{3 \times 3}$:

$$\alpha_{3-1-3} = \begin{bmatrix} (\cos \phi \cos \psi - \sin \phi \cos \theta \sin \psi) & (\cos \phi \sin \psi + \sin \phi \cos \theta \cos \psi) & (\sin \phi \sin \theta) \\ (-\sin \phi \cos \psi - \cos \phi \cos \theta \sin \psi) & (-\sin \phi \sin \psi + \cos \phi \cos \theta \cos \psi) & (\cos \phi \sin \theta) \\ (\sin \theta \sin \psi) & (-\sin \theta \cos \psi) & (\cos \theta) \end{bmatrix} \quad (2.7)$$

where, due to the orthogonality of α ,

$$\begin{bmatrix} x \\ y \\ z \end{bmatrix} = \alpha \begin{bmatrix} X \\ Y \\ Z \end{bmatrix}, \quad \begin{bmatrix} X \\ Y \\ Z \end{bmatrix} = \alpha^T \begin{bmatrix} x \\ y \\ z \end{bmatrix} \quad (2.8a,b)$$

These three Euler angles provide an initial transformation. However, since this is a spin-stabilized spacecraft, one or more of the Euler angles are subject to change due to the rotation of the craft as well as any nutational effects (to be discussed in Section 4.6.1). Thus, the direction cosine matrix α is time-variant. These Euler angle rates are functions of the body rates based on the following relationship [5]:

$$\begin{bmatrix} \dot{\psi} \\ \dot{\theta} \\ \dot{\phi} \end{bmatrix} = \frac{1}{\sin \theta} \begin{bmatrix} \sin \phi & \cos \phi & 0 \\ \cos \phi \sin \theta & -\sin \phi \sin \theta & 0 \\ -\sin \phi \cos \theta & -\cos \phi \cos \theta & \sin \theta \end{bmatrix} \begin{bmatrix} \omega_x \\ \omega_y \\ \omega_z \end{bmatrix} \quad (2.9)$$

This direction cosine matrix is calculated on a real-time basis assuming full-state navigational feedback. This information is provided by star trackers, which are discussed in further detail in Section 3.2.

2.4 Orbital Control Overview

Typically, the maneuvering of spin-stabilized satellites is done via open-loop control; the desired change in velocity ΔV is divided by the acceleration capabilities of the thrusters, a_{avail} , to obtain the expected “burn” time t_{burn} :

$$\frac{\Delta V}{a_{avail}} = \Delta t = t_{burn} \quad (2.10)$$

However, because the MMS spacecraft are spinning about an axis, as depicted in Figure 2-3 [9], the thrust vector is almost never perfectly aligned with the radial error vector, as seen from Figure 2-4, and therefore a correction factor must be included.

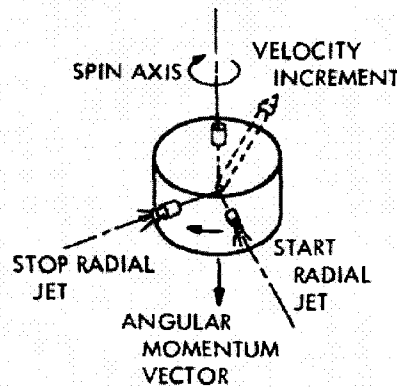


Figure 2-3: Radial thrust visualization, depicting starting and stopping points of the radial thruster

This correction factor is related to the intended burn angle window (i.e. the angle defined by the start and end of the radial thrust) and has a direct and significant impact upon the available acceleration of the thrusters. With the correction factor in place, Equation 2.10 becomes

$$\frac{\Delta V}{\kappa \cdot a_{avail}} = \Delta t = t_{burn} \quad (2.10a)$$

Specifically, the term κ relates to the cosine of the burn angle window, 2β , as seen from Figure 2-4. This factor is always less than one for a spin-stabilized spacecraft and will thus increase the amount of burn time necessary for a given ΔV maneuver.

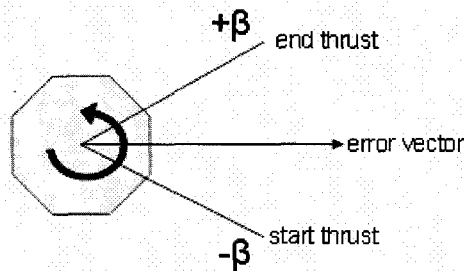


Figure 2-4: Radial burn angle window 2β as seen from inertial frame perspective

The onboard sensing capabilities of the MMS spacecraft are limited to only translational acceleration (via an accelerometer) and attitude (via a star tracker). The actuating capabilities are limited to on-off thrusters. However, the alignment of the thrusters on the spacecraft allows for both translational and rotational control. For the purposes of this research, no rotational or attitude control (i.e. torsional control) is considered possible but rather the negative effects from improper or inexact control is included as a disturbance. These sensors and actuators are discussed in more detail in the following section.

CHAPTER 3

FLIGHT HARDWARE

Various hardware systems need to be taken into account when creating an accurate model of a satellite and its capabilities. Among these systems are the sensors and actuators aboard the spacecraft. The MMS mission designers seek to use minimal sensor systems in order to save weight (and therefore costs), and thus there are only three primary hardware systems aboard the spacecraft which directly affect the control of each individual satellite. These systems are the accelerometers, star trackers and the thrusters.

3.1 Accelerometers

Accelerometers aboard a spacecraft are capable of measuring translational acceleration. For the purposes of this research, the accelerometers provide the controller with velocity and position feedback by integrating the accelerometer signal. For the sake of accuracy, the accelerometer model block includes noise and bias levels based upon typical values for this application in addition to an inherent time delay due to noise filtering. The MMS spacecraft are predicted to have one 3-axis accelerometer each, although for reliability and ease of operations, this number may increase to two per spacecraft. For the purposes of this research, a noise model with bias is included into all acceleration measurements, which will test the controller's robustness and ability to negate noise and drift due to measurement integration.

3.2 Star Trackers

Star trackers and star sensors are light-sensing devices which, when mounted to the face of a spacecraft, can detect the arrangement and magnitude of stars and determine the attitude (i.e. orientation) of the spacecraft based upon star field databases. These databases are usually onboard the spacecraft and contain references to the position and magnitude of stars and constellations. Many of these devices are complex cameras which can image large areas of space for more detailed readings and thus typically have very high accuracies. Star trackers will enable attitude determination aboard the MMS spacecraft. Each MMS spacecraft will have one star tracker. For the purposes of this research, no noise model has been added to any attitude measurements.

3.3 Thrusters

Satellite thrusters are typically cold-gas thrusters which emit small bursts of propellant for lateral and rotational impulse movements. Thrusters are generally arranged in layouts that allow for ease and access of control. In general, the thrusters used on spacecraft are on-off or “bang-bang” actuators; the thrusters are capable of only one level of force. The thrusters employed on the MMS spacecraft will most likely be mono-propellant hydrazine thrusters. There will be twelve of these thrusters, arranged such that there are two facing the +Z axis, two facing the -Z axis, four facing the -Y axis and four facing the +Y axis. Because the spacecraft are spin-stabilized, the + and -Y thrusters are the only available radial actuators and will handle all non-axial maneuvers. This research simplifies the thruster model such that there is only one actuator in each of these axes. Any minimum firing times must also be taken into account when using thruster burns.

For the purposes of this research, a minimum firing time of 20ms is assumed and a bias will be included to further investigate the controller's robustness.

CHAPTER 4

SYSTEM DESIGN

A majority of the work done on this research has been focused upon the creation of a simplified but relatively accurate model of the satellite and its environment. The system can be divided into its major components: satellite model and inputs, thruster model, coordinate transformations, controller design, sensor and noise models, and relevant disturbances. This section examines each component and presents all assumptions in this research.

4.1 Satellite Model and Inputs

For the mathematical model of the satellite and the equations of motion that describe the system, it is assumed that rigid body motion is sufficient. (i.e. No flexible structures are taken into account in this research.) As such, the equation of motion of the spacecraft is:

$$\ddot{\vec{x}} = \frac{1}{m} \cdot \vec{F}_{thrust} + \vec{g} \quad (4.1)$$

where \vec{F}_{thrust} is the force vector due to the satellite thrust and \vec{g} is the acceleration vector due to gravity, given by:

$$\vec{g} = -\frac{\mu}{|r|^2} \cdot \vec{r} \quad (4.2)$$

Here, \vec{r} represents the position vector in x-y-z coordinates with respect to Earth, and the term μ is Earth's gravitational constant. It is important to note that the acceleration term from equation 4.1 is not obtained directly, but is measured with the accelerometers described in Section 3.1. As such, it is necessary to include the sensor model (with noise and bias) into the system using the specifications which will be listed in Section 4.5.

All system inputs are in the form of ephemeris data for the MMS spacecraft, which are converted into Cartesian position and velocity vectors and assigned as initial conditions to two spacecraft models in Simulink. One of these spacecraft models is the true model which is acted upon by the thrusters and forced around an orbit by gravity. The other model is referred to as the target spacecraft. The difference between these two models is that a prescribed velocity difference vector $\Delta\vec{V}$ is added to the target spacecraft's initial velocity condition. (In orbital dynamics, orbit transfers are almost always defined in terms of the amount and direction of ΔV necessary to change from an initial orbit to a desired orbit.) In physical terms, the two spacecraft models begin at the same point but are "heading" in different directions by the ΔV amount. The only force acting upon the target model is gravity. After the simulation begins, the target spacecraft's position and velocity vectors are continually uploaded to the true model and an error vector is generated by finding the difference between the two models' position and velocity vectors. This error vector is defined as:

$$\vec{e} = \begin{bmatrix} e_{pos,r} \\ e_{pos,a} \\ e_{vel,r} \\ e_{vel,a} \end{bmatrix} \quad (4.3)$$

where the subscripts r and a represent the radial and axial components, respectively.

4.2 Thruster Model

The accuracy of the thruster model in MATLAB/Simulink is crucial to acquiring relevant and accurate data. Since the thrusters on the true spacecraft are limited in capabilities, as described in Section 3.3, any modeling of the thrusters in Simulink must take into account those limitations with extreme accuracy. In this case the thrusters are a “bang-bang” actuator with one level of thrust output. Also, the simulated timing of the thrusts based on the nominal burn angle is critical as it mirrors the true processes that are inherent actual satellite thrusters. Along with the natural thruster behavior, thruster disturbances must also be included into the model as per the specifications of either NASA GSFC or the manufacturers. These disturbances are introduced in Section 4.6.

The Simulink model of the thrusters consists simply of a “sign” function coupled with a gain block, as shown in Figure 4-1. Here, u is the output of the controller. The specifics of the controller are discussed in Section 4.4. The output from the gain, F_t , is the actual thrust force that acts as a forcing input to the system dynamics.

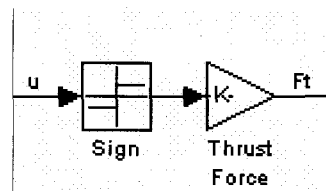


Figure 4-1: Simulink thruster model

4.3 Coordinate Transformations

As stated in Section 2.2, there are several reference frames that are used throughout the simulation and it is important to identify where these conversions between frames take place. The first conversion occurs outside of the Simulink model in the MATLAB code itself. Here, the desired ΔV vector, initially defined in terms of the orbital

coordinate system (OCS, from Section 2.2.3), is converted into the inertial frame of Earth. In order to define the ΔV vector, it is first necessary to establish the OCS. The unit vector along the x_o -axis is defined as equal to the initial velocity vector. The x_o -axis is referred to as the “in-track” direction. The unit vector along the z_o -axis is defined as:

$$\hat{z}_o = [0 \quad -\sin(i) \quad \cos(i)]^T \quad (4.4)$$

where i is the orbital inclination. This axis is referred to as the “orbit-normal” direction. Finally, to complete the orthogonal triad, the unit vector along the y_o -axis is defined as the cross-product of the unit vectors along the x_o - and z_o -axes:

$$\hat{y}_o = \hat{x}_o \times \hat{z}_o \quad (4.5)$$

The y_o -axis is referred to as the “cross-track” direction.

Because there are only two body directions in which the satellite can actuate—radial and axial—it is necessary to convert the body-frame Cartesian x and y errors into equivalent cylindrical coordinates (radius and angle) by using the following equations:

$$r = \sqrt{x^2 + y^2} \quad (4.6a)$$

$$\theta = \tan^{-1}\left(\frac{y}{x}\right) \quad (4.6b)$$

The term r refers to the magnitude and θ to the angle to r in the plane of rotation. The axial direction is equated with the z coordinate.

4.4 Controller Design

4.4.1 PID Gain Selection

The design of the controller for this system began by using a simple PID control with the input being the position and velocity errors in radial and axial components. This would require that each of the P, I and D $\in \mathbb{R}^{2 \times 4}$. Note that in the early stages of development, the controller ignored both the fact that the thruster model is an on-off control with only one magnitude of force available and also that the satellite was spinning. Using the results of this simplified system as a basis for comparison, the complexities of both the actuator and the spinning spacecraft were incorporated into the system model. It was quickly seen that the previous PID control design would not be capable of accurately driving the errors towards zero. The problem of primary concern, depicted in Figure 4-2, is that when a smoothly decreasing control signal is applied to the thruster model from Figure 4-1, the actuators deliver excessive amounts of thrust into the system plant, effectively overcompensating for the duration of the control cycle.

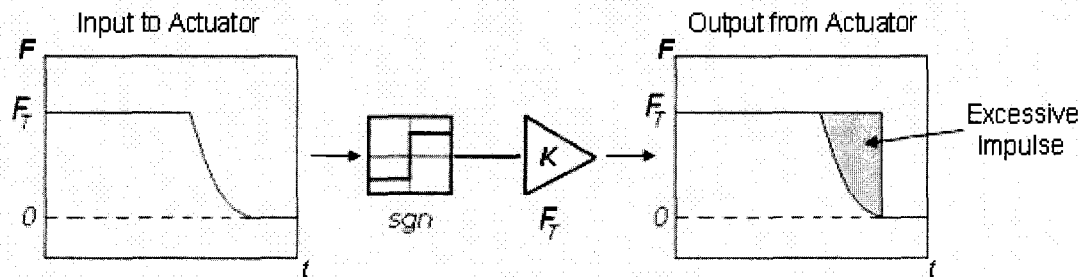


Figure 4-2: Result from sending smooth control signals into the actuator model

From this problem came the realization that in order to accurately control the errors, the input signal to the thruster model must be as close as possible to the desired output of the thruster model (i.e. the thruster model effectively makes no changes to its input signal). This essentially requires that the input to the thruster model is a square wave or series of square waves with amplitudes equal to the available thrust force F_T . To this end the control gains in the PID matrices were reevaluated and tuned appropriately and the raw output signal from the control block is manipulated, by use of a hysteresis relay, such that it precisely resembled the capable output from the thruster model.

The final gain matrices are shown in Table 4.1. Several factors decided the final gain selection, including the desired velocity error percentage, the semi-major axis criterion, the allowable fuel efficiency, and the control signal that is sent into the thruster model. In traditional control design, a higher proportional (P) gain on the velocity is necessary to drive the velocity error to zero as quickly as possible. By referring to the SMA derivation in Equation 2.6, it was determined that the velocity errors, both axial and radial, should be weighted much more heavily than the position errors. Taking both of these considerations into account, the gains proportional to the velocity errors are many orders of magnitude greater than the gains on the integral of the velocity. The final gain values were arrived at by tuning the initial values. No gain on the derivative of the velocity was seen to be necessary or fuel efficient. Although the gain values on the velocity errors are quite large, the signal is saturated before being sent into the thruster model so that the maximum value is $\pm F_T$.

	Position Errors		Velocity Errors	
	radial	axial	radial	axial
P	0	0	10000	0
	0	0	0	10000
I	0	0	0.15	0
	0	0	0	0.15
D	0	0	0	0
	0	0	0	0

Table 4.1: PID gain matrices

A simplified diagram of the major simulation blocks is shown in Figure 4.3. This diagram includes the thruster model, system and sensor dynamics, gravitational acceleration and the calculation of accumulated ΔV (considered the “fuel use” of the controller). Missing from this diagram are all coordinate transformations and shutoff and timing mechanism.

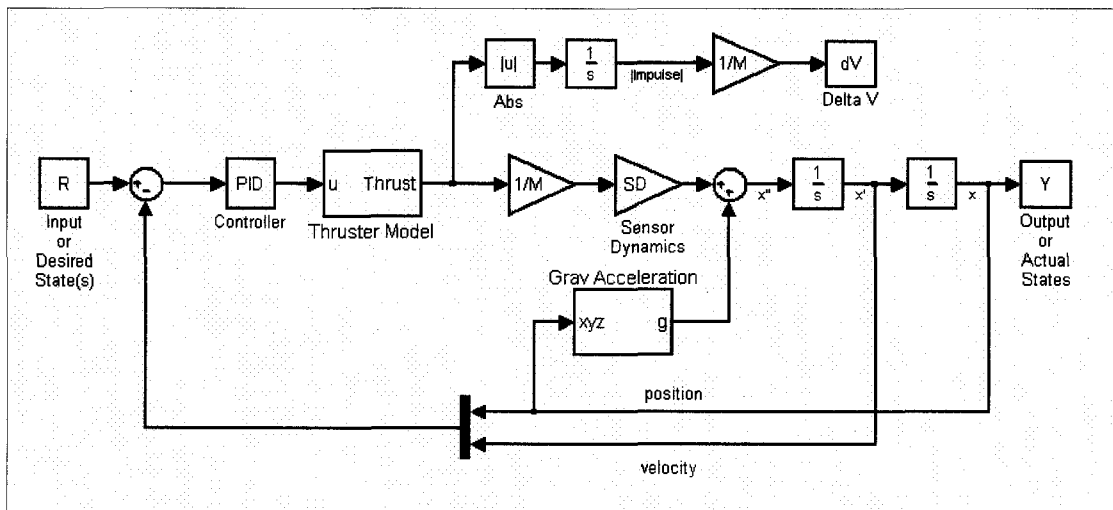


Figure 4-3: Simple representation of the main system dynamics and simulation blocks

4.4.2 Radial Thruster Timing

The next consideration is timing the radial firing such that the radial thrusters only fire within the allowed burn angle window 2β (as in Figure 2-4). This is done using flags and switching blocks in the Simulink model. When the body-frame x- and y-errors are converted into cylindrical coordinates (Equations 4.6a and b), the associated angle of the error vector, θ_e , is used as a reference. Since the MMS spacecraft utilize two pairs of radial thrusters on opposite faces of the craft, the radial thrusters are allowed to fire twice per spin. In order to time both burns accurately using only the error angle θ , it is necessary to make use of a trigonometric function that repeats only twice per cycle. Fortunately, the absolute value of the tangent of the error angle will provide the necessary flag criteria. Since the tangent function repeats twice per cycle, as seen in Figure 4-4, it is possible to set a limiting value L where:

$$L = \tan(\beta) \quad (4.7)$$

such that the control signal for the radial thrusters is allowed to pass to the thruster model only when:

$$\frac{|\tan(\theta)|}{\tan(\beta)} \leq 1 \quad (4.8)$$

This algorithm ensures that the radial thrusters fire only when within the intended burn angle window 2β .

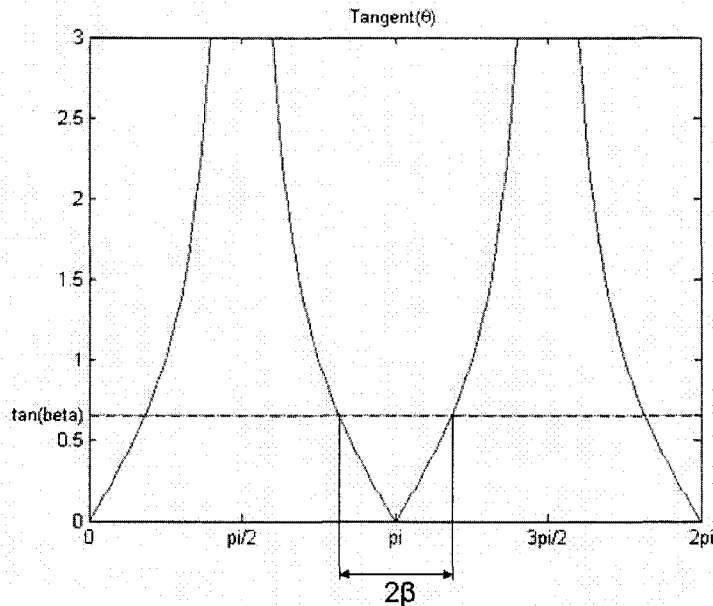


Figure 4-4: Tangent of firing window β provides timing algorithm for radial burns

Also note that throughout the course of an actual orbit transfer, NASA flight dynamics analysis engineers plan to reduce this firing window by an (as-yet) unknown amount. The condition for reducing this firing window is a ΔV threshold; when the ΔV error reaches a certain percentage of the initial value, the allowable firing angle is reduced by a certain percentage. This condition is included in this simulation by use of switches. Arbitrary values for both the ΔV threshold and the amount of angle reduction are used in order to gauge any potential side-effects of this reduction.

4.4.3 Axial Thruster Timing

Unlike the radial thrusters, the axial thrusters are allowed to burn continuously for an indefinite amount of time. However, testing has shown that, because disturbances and misalignments increase the error in the axial direction over time, it is better to pause all axial corrections after a short amount of time. After this pause the axial thrusters can

again correct any lingering errors. There are two reasons for this: first, it is likely that nutation in the system will result in “perceived” errors that may cause the axial thrusters to burn unnecessarily (Section 4.6.1 describes nutation in more detail). These faulty corrections result in wasted fuel, thus it is more efficient to include this delay. Also, by implementing a pause in the axial correction, the system reduces the amount of axial corrections made and instead will often make one final, larger adjustment towards the end of the maneuver. Reducing the amount of corrections will have a positive impact on future studies of the MMS spacecraft, which will investigate flexible structures and modes of vibration. Large amounts of impulses can create excessive vibration problems and thus the flight dynamics analysis engineers hope to avoid this issue altogether.

4.4.4 Shutoff Criteria

This system makes use of switches which cease all thruster control, both axial and radial, upon reaching certain error threshold values. The reason for utilizing these threshold values—or shutoff criteria—is that one of the parameters that the system is trying to minimize is the semi-major axis error. Although the SMA error is a function of both the position and velocity error magnitudes, it is not always clear how the SMA error is affected by a combination of in-track, cross-track and orbit-normal ΔV components. It has been determined during testing that it is possible to have a low velocity error and relatively high SMA error and vice versa. Thus, in order to ensure that both conditions are met, the system makes use of a double-success shutoff in which all thruster control ceases when, and only when, the SMA error is within 50 meters and the velocity error is within 1%. It is assumed in this research that this type of abrupt shutoff is possible on

board the actual satellite, with respect to the delays in knowledge of errors and calculation of the semi-major axis, etc.

4.4.5 Hysteresis Relays

In addition to the linear PID controller and timing switches previously mentioned, the controller also makes use of relays with hysteresis levels. This block occurs directly before the thruster model. Relays output only one value based upon the value of the input. For the purposes of this controller, the output is set to the available thrust force F_T . Hysteresis is included in the relay to provide an envelope around the errors—an envelope in which those errors will be ignored so as to help allay some of the side effects of nutation, mentioned in Section 4.4.3, in which errors are perceived to be higher than they actually are. By using a hysteresis level, any error inside the envelope is ignored, as stated, and if the errors exceed this envelope, the thrusters actively correct the errors until they are again zero. Figure 4-5 depicts the behavior of the relay block and the result of including hysteresis. Here, the envelope of error ignored by the system is $\pm c$.

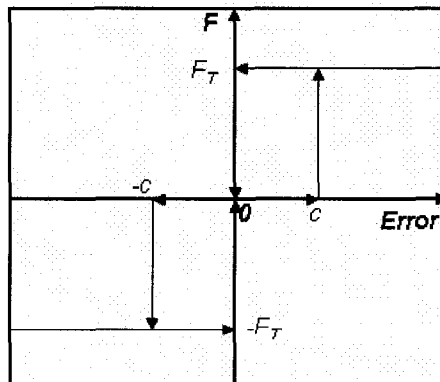


Figure 4-5: Depiction of relay with hysteresis

4.5 Sensor and Noise Models

Based upon specifications from GSFC, an accelerometer noise model was developed by Dean Tsai of NASA GSFC using standard Butterworth filters. The objective was to create a power density spectrum (PSD) which closely resembles that of a standard accelerometer used in this environment. Tsai's model is shown in Figure 4-6. Using Welch's method, the PSD from Tsai's filtered accelerometer noise model was captured and is shown in Figure 4-7.

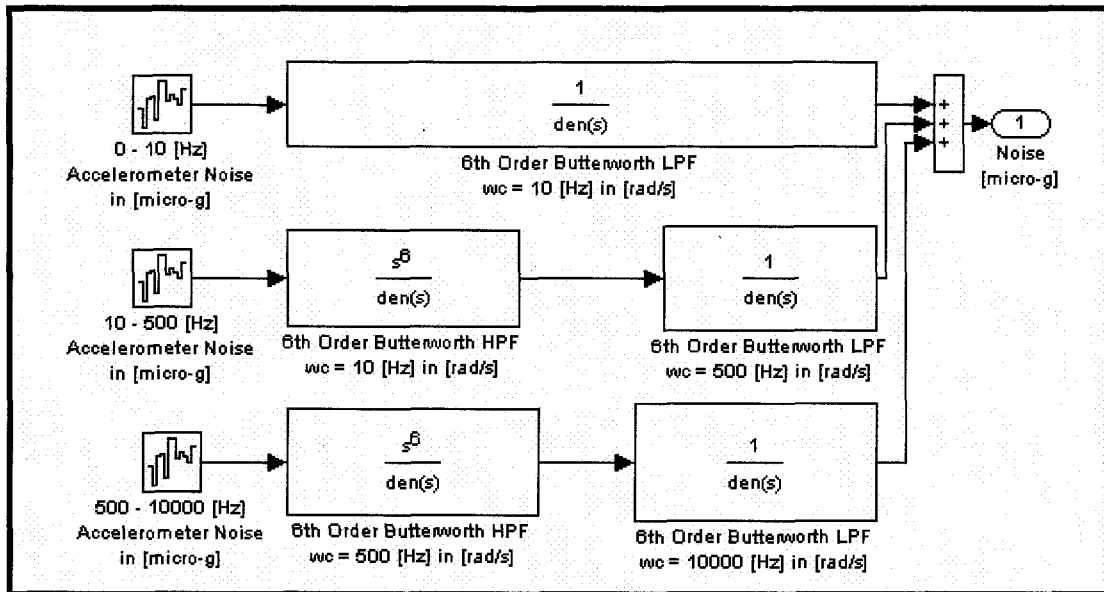


Figure 4-6: Dean Tsai's accelerometer noise model, using three frequency ranges and Butterworth filters

With this model and PSD as a basis, a new, simpler noise model was constructed using only a band-limited white noise block and a first-order filter. This was done to lessen the length of simulation time, since the "true" model—the noise model developed by Dean Tsai—requires a simulation time step of $10\mu\text{s}$, based on the principle of having a

time step of one order of magnitude higher than the largest frequency. The filter of this simpler model has a break frequency of 200Hz which requires a much larger time step of 500 μ s, allowing for faster testing. In order to ensure that the simpler noise model is conservative, the power levels from the PSD of the filtered model must at least be as high as those from Tsai's model across the frequency spectrum. This comparison is shown in Figure 4-8. From this it is seen that the simpler model is adequate and can be used as a conservative estimate.

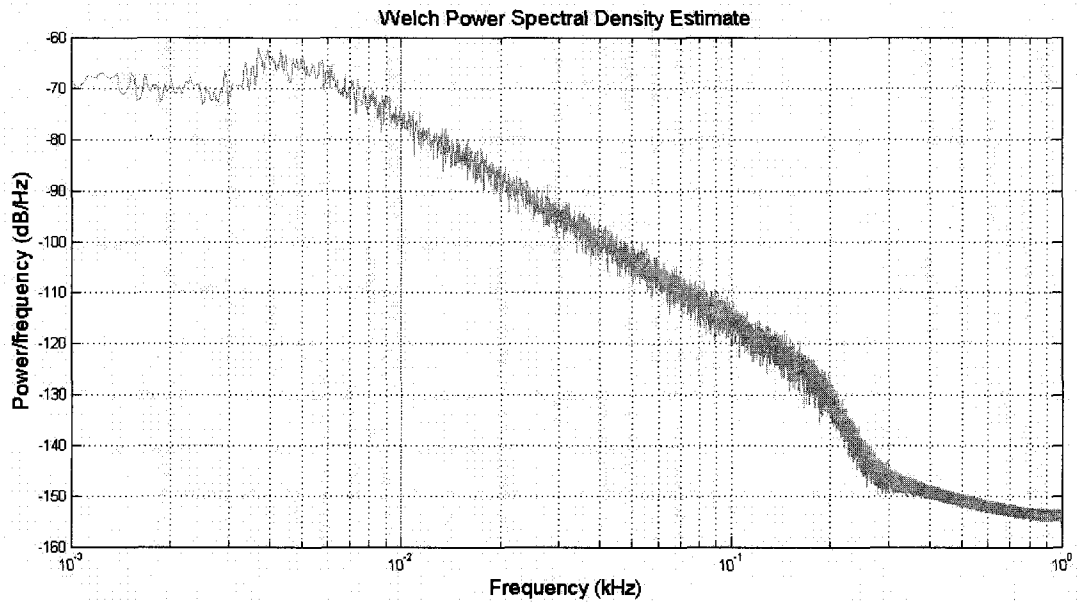


Figure 4-7: Power Density Spectrum from the "true" accelerometer noise model

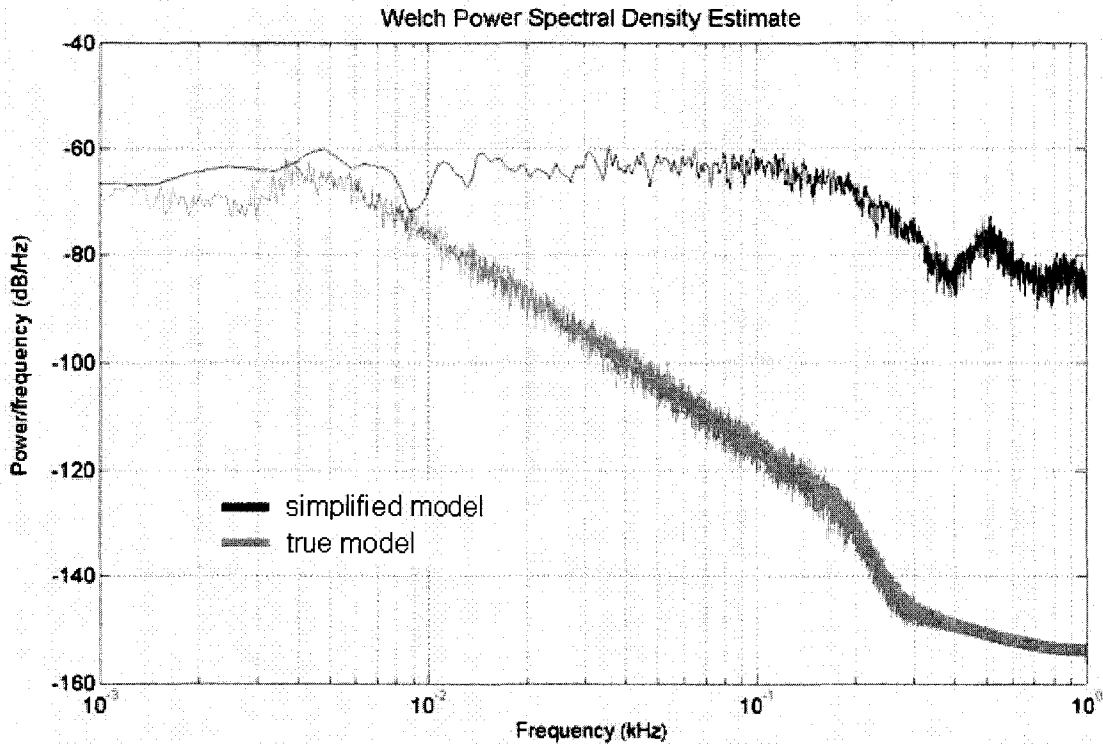


Figure 4-8: Comparison of PSD plots from “true” and simplified noise models

4.6 Relevant Disturbances

This research considers three main disturbance factors to the system: nutation, thruster misalignment and sine (or “off-directional”) components of the radial thrust. Each has a distinct effect on the system and all have been parameterized according to either relevant research or specifications given by NASA GSFC engineers.

4.6.1 Nutation

Nutation is defined by Wertz [4] as “rotational motion for which the instantaneous rotation axis is not aligned with a principle axis.” Such types of impure rotation arise from various causes, ranging from thruster imbalances to misalignments between the angular momentum vector and the principle axis of rotation. This research does not infer

a cause for the nutation but rather includes the undesired product of such impurities into the system as simply a rotation rate about a secondary axis. The specification to which this disturbance is held is in the form of a nutation angle, which measures the deviation of the angular momentum vector L from the spin axis, as shown in Figure 4-9. Specifications for the MMS mission require at least 0.35° nutation angle stability for normal operation.

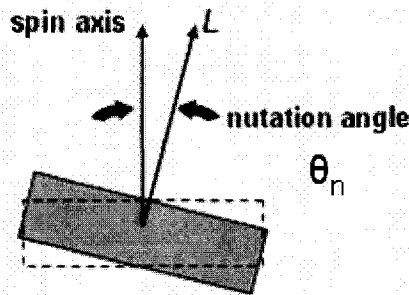


Figure 4-9: Nutation angle requirement θ_n

To determine what this requirement means in terms of a secondary axis rotation rate, Equation 4.9 is employed:

$$\tan(\theta_n) = \frac{L_{non-spin-axis}}{L_{spin-axis}} = \left(\frac{\sqrt{(I_{xx} \cdot \omega_x)^2 + (I_{yy} \cdot \omega_y)^2}}{I_{zz} \cdot \omega_z} \right) \quad (4.9)$$

where L is the angular momentum scalar, ω_i is the rotational rate in the i -axis, and I_{ii} is the moment of inertia in the i -axis. Equation 4.9 can be simplified to Equation 4.10 by assuming only one secondary rotational rate (here, only ω_x) and using a small angle approximation:

$$\theta_n \approx \left(\frac{I_{xx} \cdot \omega_x}{I_{zz} \cdot \omega_z} \right) \quad (4.10)$$

Using a nutation angle of $\theta_n = 0.35^\circ = 0.061rad$ and moments of inertia $I_{xx} = 2379kg \cdot m^2$ and $I_{zz} = 4201kg \cdot m^2$, it is calculated that ω_x must be 1.11% of the nominal spin rate ω_z . This conservative secondary spin rate is used throughout the research whenever nutation is included.

4.6.2 Thruster Bias and Misalignments

When creating a model of a satellite actuating system, it is necessary to include the possibility of bias levels of thrust and misalignments between thrusters. Here, only misalignments between radial and axial thrusters are considered, ignoring the possibility of radial-radial or axial-axial imbalances. The latter type of thruster disturbances tends to result in either nutation rates, which are already considered, or in changes in nominal spin rates due to a net torque about the principle axis, which this research does not consider.

According to specifications from NASA GSFC, the system must allow for a 5% thruster bias and 1° misalignment between the radial and axial thrusters. Misalignments between thrusters have the effect of adding unwanted thrust into the perpendicular direction as well as reducing the thrust in the intended direction. It has been determined that the worst-case scenario is one in which the radial thrusters are misaligned by 1° towards the axial direction and is thus the conservative scenario that this research assumes.

4.6.3 Sine Component of Radial Thrust

As mentioned in Section 2.4, the radial thrust is almost never aligned with the desired thrusting direction due to the nominal spin rate of the spacecraft. Because of this it is necessary to consider both the sine and cosine components of the radial thrust, in relation

to the error vector. As seen from Figure 4-10, each period of radial thrust begins at angle $-\beta$ from the true error direction and ends at angle $+\beta$. This “window of radial firing” (i.e. 2β) is preset according to analyses by GSFC and its effect on the system is twofold: clearly, the size of this predefined window has an effect on the overall efficiency of the orbital transfer maneuver; the larger the allowed window, the more fuel is wasted in each burn due to imperfect alignments. The thrust performed in the intended direction is referred to as the “cosine component” of the radial thrust. Secondly, the fuel that is “wasted” is propelling the satellite in a direction perpendicular to the intended thrust direction and must be taken into account. This is what is referred to as the “sine component” of the radial thrust. Ideally, the perpendicular propulsion from one side of the burn cancels out with the propulsion from the opposite side, but the simulation must allow for a potential lopsided burn, favoring either the $+\beta$ or $-\beta$ side.

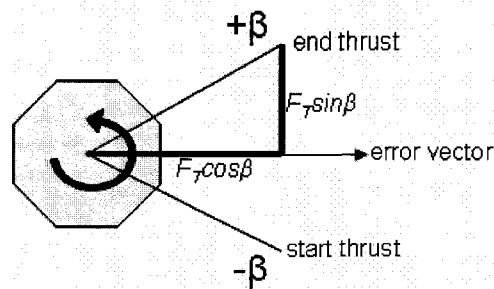


Figure 4-10: Sine and cosine components of radial thrust for a given θ_e

CHAPTER 5

RESULTS

The results from various simulation testing scenarios are presented here. These results are divided into several studies in which the disturbances are individually introduced into the system so that the effects of each disturbance can be compared to the ideal case. Next, the disturbances are included all together for a worst-case study and all studies hereafter are assumed to be this most conservative case. Until this point all cases have been studied assuming only one particular orientation, which is initially aligned with the Earth inertial frame. The next study tests the controller for any sensitivity to various orientations.

As stated, the previous case studies utilize the double-success shutoff described in Section 4.4.3. However, it is possible that only one of these two parameters—SMA error or ΔV error—can be used as a shutoff criterion. In preparation for this more limiting scenario, the next two cases examine the viability of using only one of the parameters each in terms of overall success. Next, the results from using the linear controller are compared to results using a more complicated nonlinear controller. Lastly, the effect of accelerometer bias levels is examined in terms of the corruption of results. Note that in all studies, the simplified noise model from Section 4.5 is included and the sine and cosine components of the radial thrust are taken into account.

The results from the first five studies are shown by way of three main figures and one table, with the first figure being a series of subplots. The three subplots in the first figure are:

- the position errors over time with respect to the inertial frame (upper left corner)
- the velocity errors over time with respect to the inertial frame (upper right corner)
- and the ΔV of both axial and radial thrusters over time with respect to the body frame of the satellite (bottom)

The tables that follow highlight the major results from each case. The second main figure shows the behavior of the SMA error over time. The third and last figure shows the radial thrust profile (top) and the axial thrust profile (bottom) for each case.

5.1 Study One: Ideal Case

Without the inclusion of nutation, in the form of secondary-axis spin rates, or any thruster misalignments or biases, the system is successfully controlled to both the SMA and ΔV criteria. Figure 5-1 shows the behavior of the inertial position and velocity errors, as well as the ΔV used by both the radial and axial thrusters compared to desired values, shown as horizontal lines. Table 5.1 shows that both of the success criteria were met, as well as the condition that no more than 90% of fuel is used per maneuver with respect to ΔV . The stepping motion of the x- and y-velocity errors as well as the actual and effective radial ΔV used is due to the pulsating behavior of the radial thrusters.

From the results table, it is seen that there is about a 5% loss of efficiency from the radial thrusters, seen in the “Delta-V Used” plot as the difference between the effective radial ΔV and the actual radial ΔV .

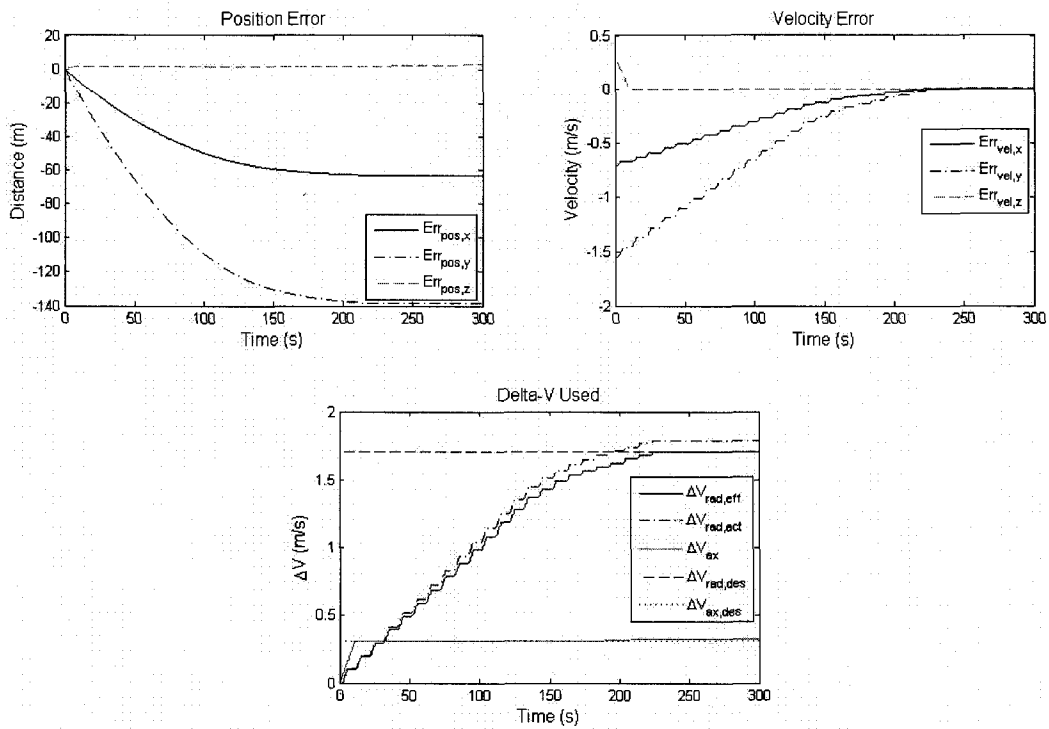


Figure 5-1: Position error, velocity error, ΔV used and major results for the ideal case

IDEAL	
Simulation Results:	
Original SMA Error:	8667.2m
Final SMA Error:	9.6m
Fuel Efficiency:	
Radial:	95.27%
Axial:	93.58%
Total:	95.22%
Resultant Velocity Error:	0.09%

Table 5.1: Results from the ideal case

What is interesting is that although the criteria were met, the position error remains at some relatively steady-state value. This implies that although some positional drift has occurred in the timeframe of the maneuver, the drift is not critical to the stated success criteria and the SMA error can still be driven towards zero. It has been determined that

this phenomenon is in part due to the importance of velocity errors in driving the SMA error to zero, but also because the multi-dimensional ΔV input has varying effects on the size of the semi-major axis. In other words a ΔV input of $[1 \ 1 \ 1]^T$ m/s means that the thrusters must burn 1m/s in each of the in-track, cross-track and orbit-normal directions. All three of these components may increase or decrease the orbit's semi-major axis, depending on the component's direction with respect to Earth. This behavior can be seen in Figure 5-2, which shows the SMA error over the course of the maneuver. Note that in the initial seconds of the burn, the SMA error is not steadily decreasing, but rather increasing and decreasing, depending on which thruster is firing at that time. This issue with the SMA error raises a concern in regards to the success criteria: does a low SMA error truly imply an accurate orbital transfer maneuver? This thesis attempts to test this question in following case studies.

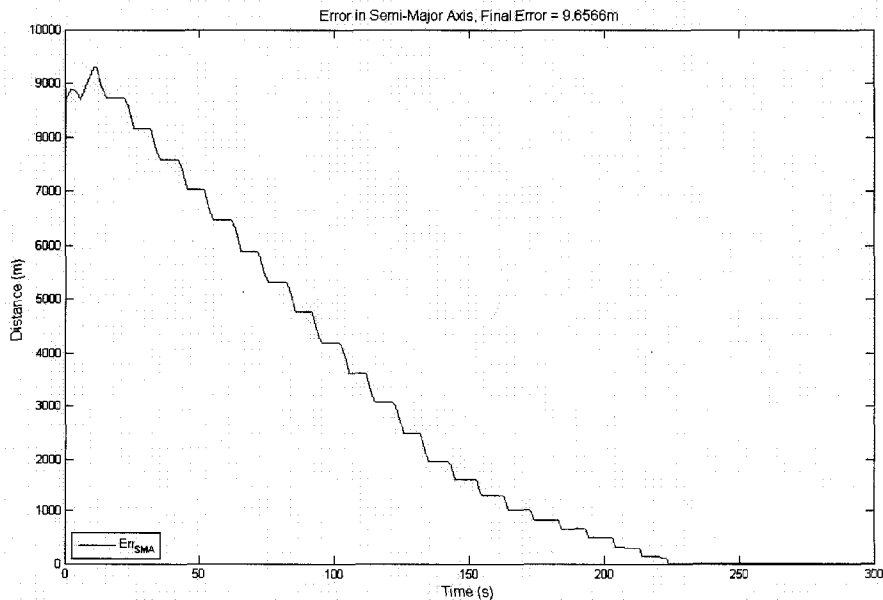


Figure 5-2: SMA error for the ideal case

Figure 5-3 shows the thruster profiles from this maneuver. The radial thrust, shown on the top, is a series of pulses of magnitude 20 Newtons and width of initially about 3.7 seconds and later about 1 second. These pulse widths are a function of the desired burn angle window 2β and the nominal spin rate ω_z . The axial thrust, shown on the bottom, shows a large initial burn and the pause immediately after. The pause is set at a nominal time of 150 seconds, after which the axial thrusters are permitted to correct any lingering errors. These final corrections are shown as the thin pulses towards the end of the axial burn.

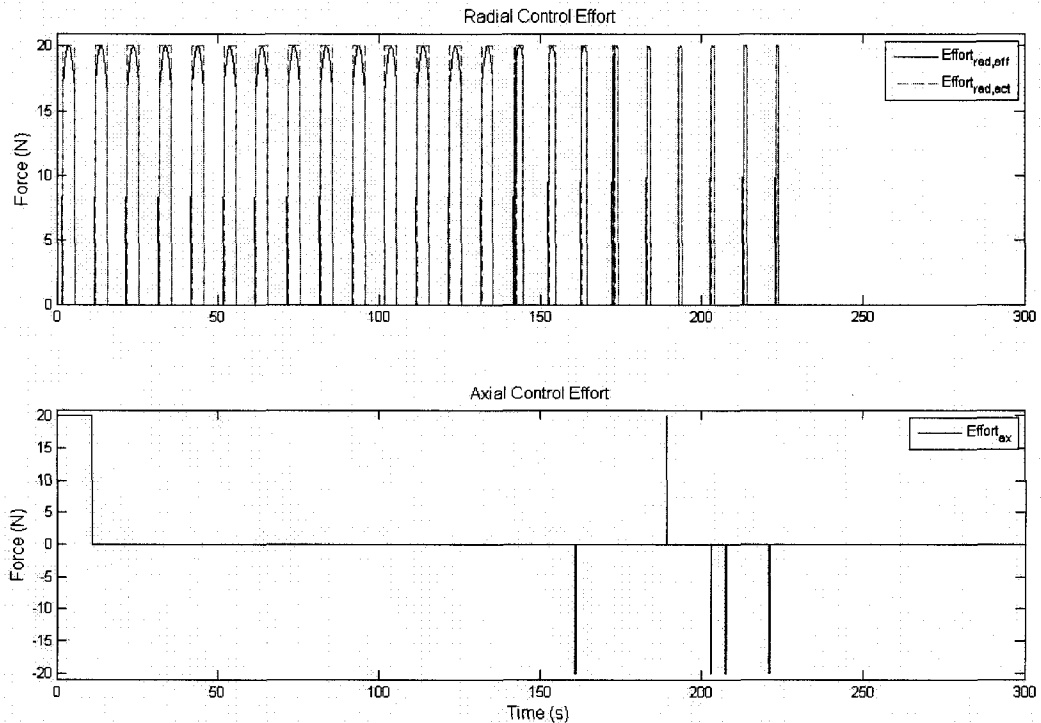


Figure 5-3: Radial and axial thrust profile for the ideal case

In a closer image of the radial burn, shown in Figure 5-4, the actual radial thrust is shown in a dotted line while the effective radial thrust is shown in a solid line. Although

the thrusters are firing continually over the course of each pulse, exemplified by the dotted line, the force seen in the direction of the error vector is curved, with maximum amplitude in the center of the pulse, shown by the solid line. At time $t = 135$ seconds, the system encounters its first ΔV threshold, which reduces the desired burn angle window. Upon reaching this threshold, the system stops radial thrust until the new burn angle window is reached at time $t = 142.5$ seconds. This abrupt cessation of the radial thrusters results in a single lopsided thrust. Although this effect does not seem to impact the errors in a significant manner, it is possible that this issue should be addressed in the future. A potential solution is to use hysteresis such that the radial burn would not abruptly stop at the first or second ΔV threshold, but rather finish the individual burn.

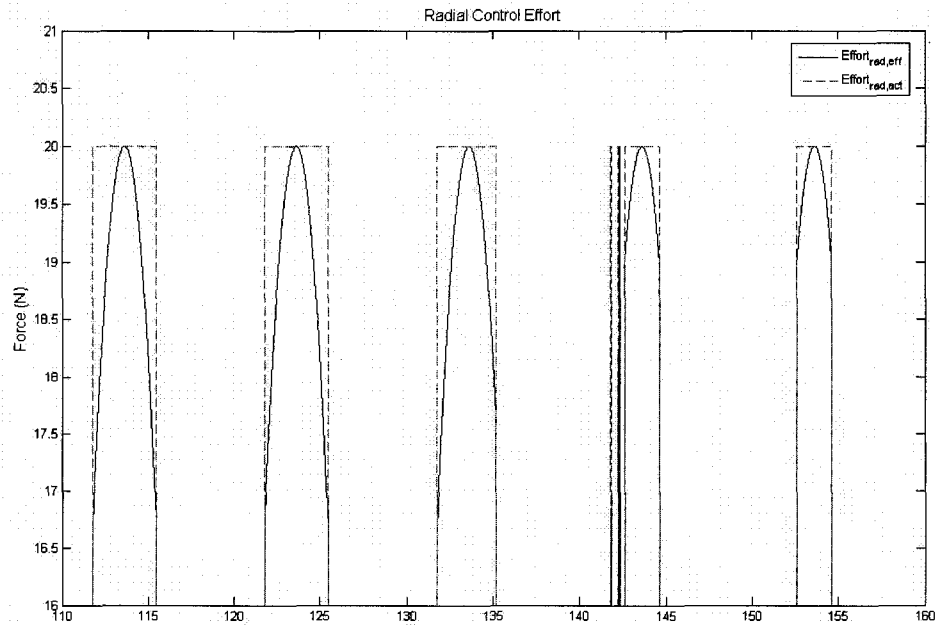


Figure 5-4: Close-up of radial thrust profile

Another concern is the series of very small impulses between times $t = 142$ seconds and $t = 142.5$ seconds. It is thought that these tiny impulses occur due to the noise in the

system; because of the accelerometer noise, the system may have a ΔV error which fluctuates between the aforementioned thresholds. This causes the system to continually change between desired burn angle windows, prompting the radial thrusters to turn off and on rapidly. Although this is an as-yet unsolved issue, it does not raise much concern primarily because the ΔV offered from these impulses are infinitesimal. In other words the impulses do not affect the system in any noticeable manner.

5.2 Study Two: Misalignments Only

The results from the second study are shown here, in which a 1° misalignment has been included between the radial and axial thrusters. Again, it has been determined through testing that the conservative case is to misalign the radial thrusters so that they bleed into the axial direction and is thus the only case considered. Figure 5-5 shows the three plots of position errors, velocity errors and ΔV used, and Table 5.2 lists the major results. Qualitatively, the results are similar to those from Study One, except that after the pause in the axial burn, there is a larger correction due to the building of errors from the misalignment. It should be noted that any efficiency losses due to the misalignment is evident in the results for the axial thrusters, albeit that these losses truly belong to the radial thrusters. Although this has the effect of artificially lowering the axial efficiency (and thus artificially raising the radial efficiency), the important value is the total efficiency of the maneuver, which is irrespective of the individual losses.

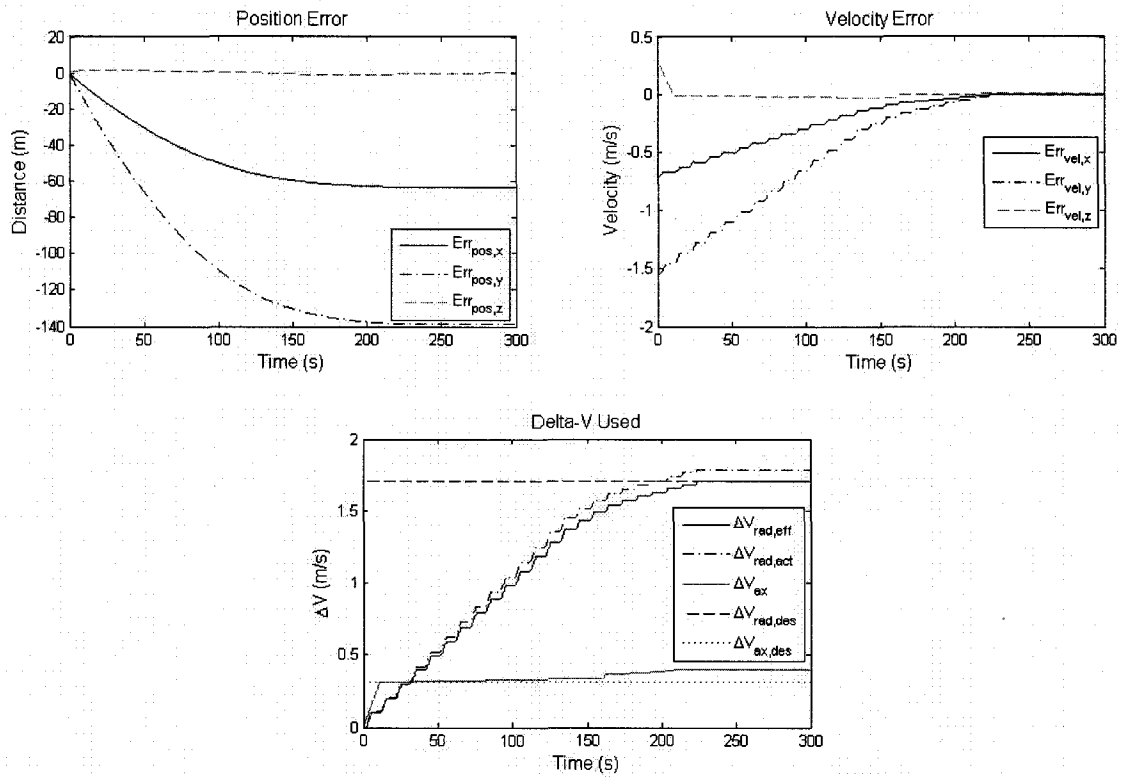


Figure 5-5: Position errors, velocity errors and ΔV used for the misalignment case.

THRUSTER MISALIGNMENT	
Simulation Results:	
Original SMA Error:	8667.2m
Final SMA Error:	5.1m
Fuel Efficiency:	
Radial:	95.28%
Axial:	78.58%
Total:	94.59%
Resultant Velocity Error:	0.09%

Table 5.2: Results from misalignment case

Figure 5-6 shows the behavior of the SMA error over the course of the maneuver. The behavior of the SMA error does not deviate much from the previous study. Figure 5-7 shows the radial and axial thrust profiles. Though the radial profile is similar to the previous case, it can be seen that during every radial impulse, there is a small impulse in the axial direction. The magnitude of these small impulses is the cosine of 1° multiplied by the thruster force F_T . After the axial pause, the large correctional burn can be seen which offsets the building of errors that has occurred from the misalignment, followed by smaller impulses for minor corrections. Quantitatively, the results from this study show successful orbital control and no major problems arise due to misalignments.

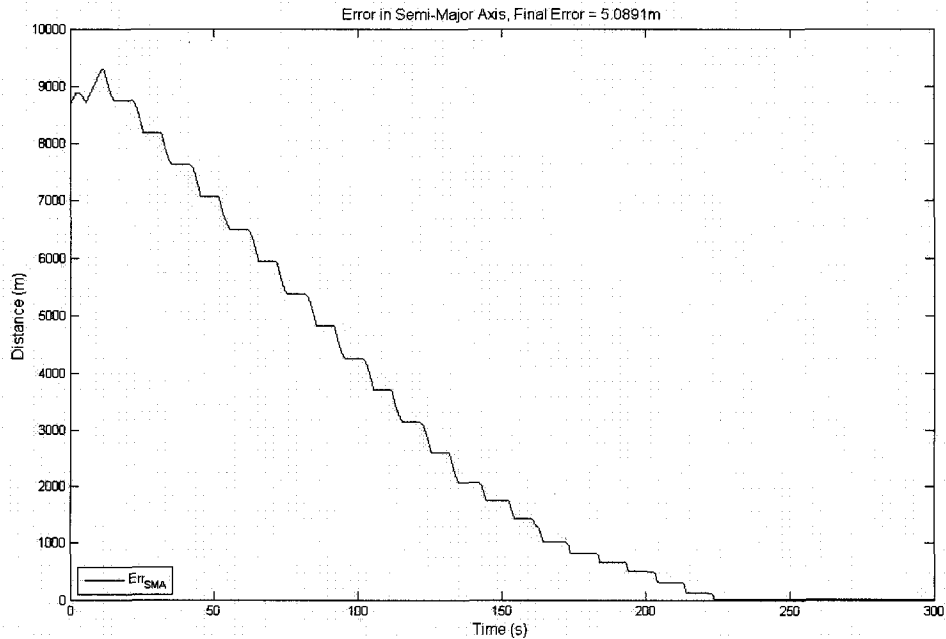


Figure 5-6: SMA error for the misalignment case

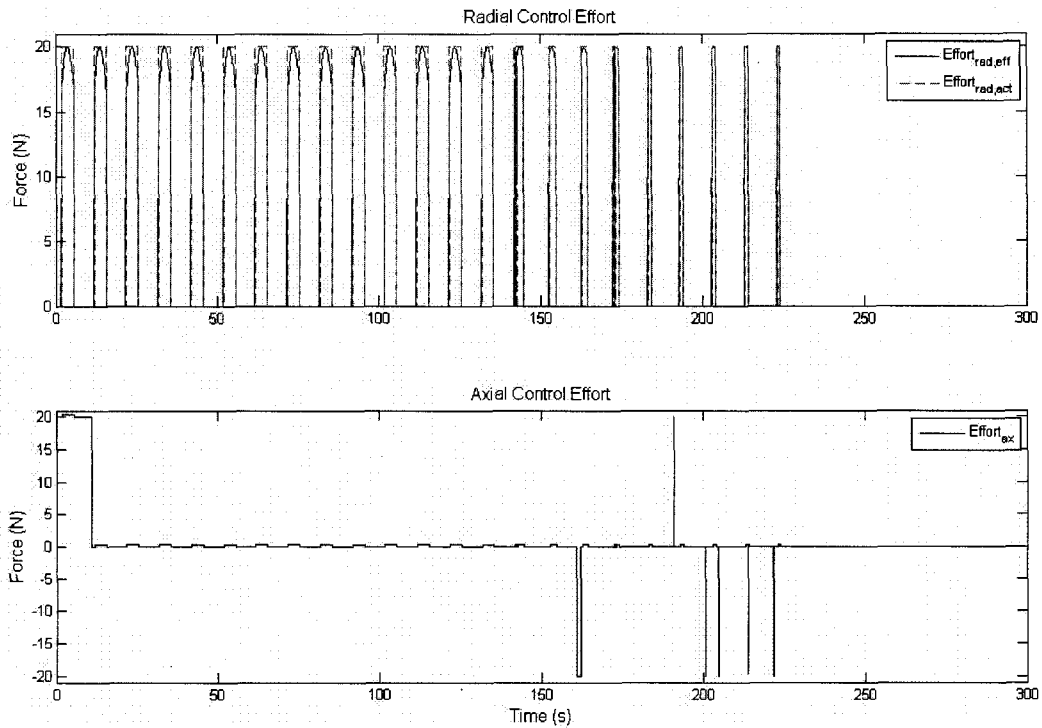


Figure 5-7: Radial and axial thrust profiles for the misalignment case

5.3 Study Three: Nutation Only

The third study considers only the inclusion of nutation into the system. It was expected that including nutation would be one of the more problematic disturbances because nutation has the adverse effect of creating errors where none exist. This happens due to the secondary rotation of the system about a minor axis, which causes the errors to oscillate with respect to the body frame. Table 5.3 shows the results from this simulation when the hysteresis relay is not included in the system. From these results it is evident that the resulting ΔV used for the axial thrusters is far more than the desired amount, which is also reflected in the tabulated results. This “wasted” impulse in the axial

direction results in a loss of overall efficiency of about 30%, which is unacceptable by mission standards.

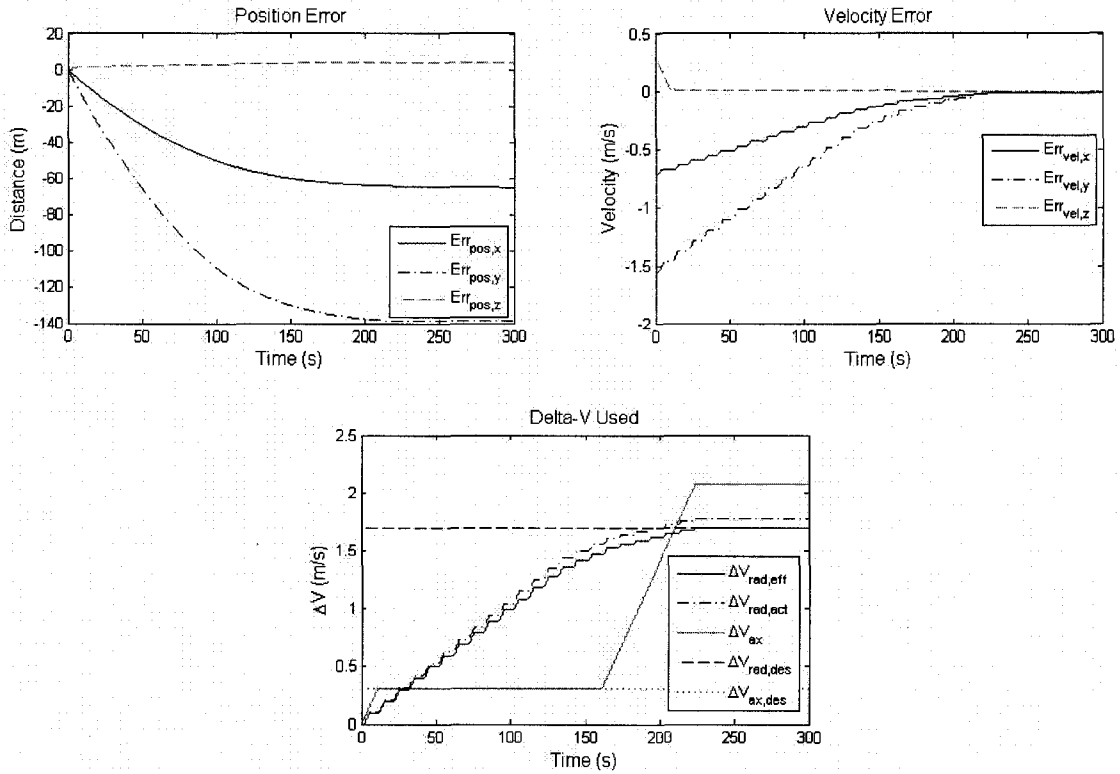


Figure 5-8: Position errors, velocity errors and ΔV used from the nutation case, no relays included

NUTATION, NO RELAY	
Simulation Results:	
Original SMA Error:	8667.2m
Final SMA Error:	6.9m
Fuel Efficiency:	
Radial:	95.29%
Axial:	14.54%
Total:	62.68%
Resultant Velocity Error:	0.09%

Table 5.3: Results from the nutation study, no relays

From Figure 5-9, which shows the thrust profile for this case, it is seen that without using relays and hysteresis, the oscillating errors induce rapid, tiny impulses from the thrusters which, though properly controlling the errors, uses far too much effort for the maneuver. These impulses appear after the nominal axial pause, from time $t = 160$ seconds until time $t = 225$ seconds. Note that noise is not included in this particular simulation to show that it is purely the nutating errors that the thrusters attempt to control.

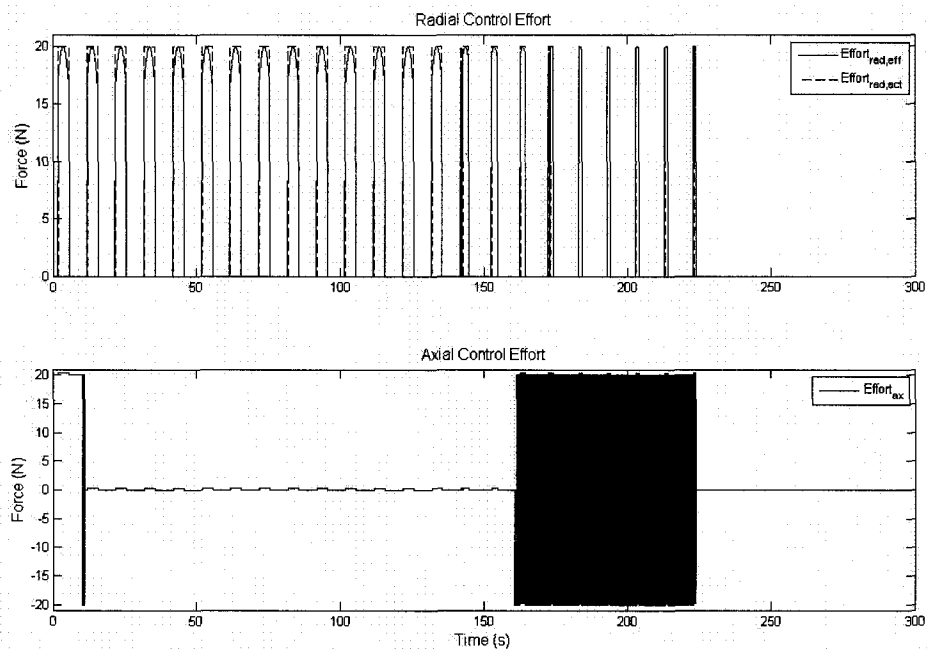


Figure 5-9: Thrust profile for the nutation case, no relays included

The previous results seem to demand a method by which the perceived errors resulting from nutation are not passed through to the thruster model. It was determined that utilizing a relay block with inherent hysteresis would provide the controller with an effective way of both ignoring nutational oscillations while still correcting lingering

errors. The following results show the improvement of the controller utilizing relays over the previous results.

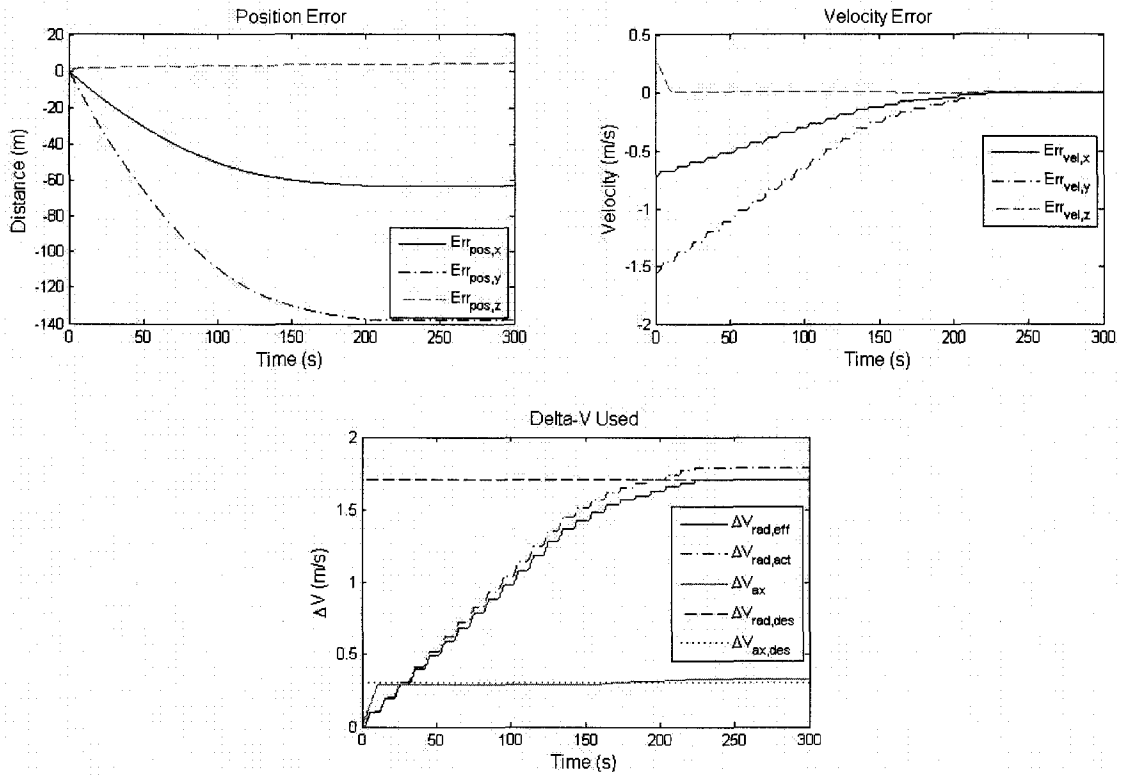


Figure 5-10: Position error, velocity error and ΔV used for the nutation case using relays

NUTATION, WITH RELAY	
Simulation Results:	
Original SMA Error:	8667.2m
Final SMA Error:	13.5m
Fuel Efficiency:	
Radial:	95.29%
Axial:	92.69%
Total:	95.21%
Resultant Velocity Error:	0.09%

Table 5.4: Results from the nutation case using relays

Figure 5-11 shows the behavior of the SMA error over the course of the burn. Figure 5-12 shows the thrust profiles for the radial and axial thrusters. Notice that the axial thruster no longer overcompensates for these perceived errors, yet the errors from Table 5.4 do not suffer because of this. More importantly, the total fuel usage remains above 90%.

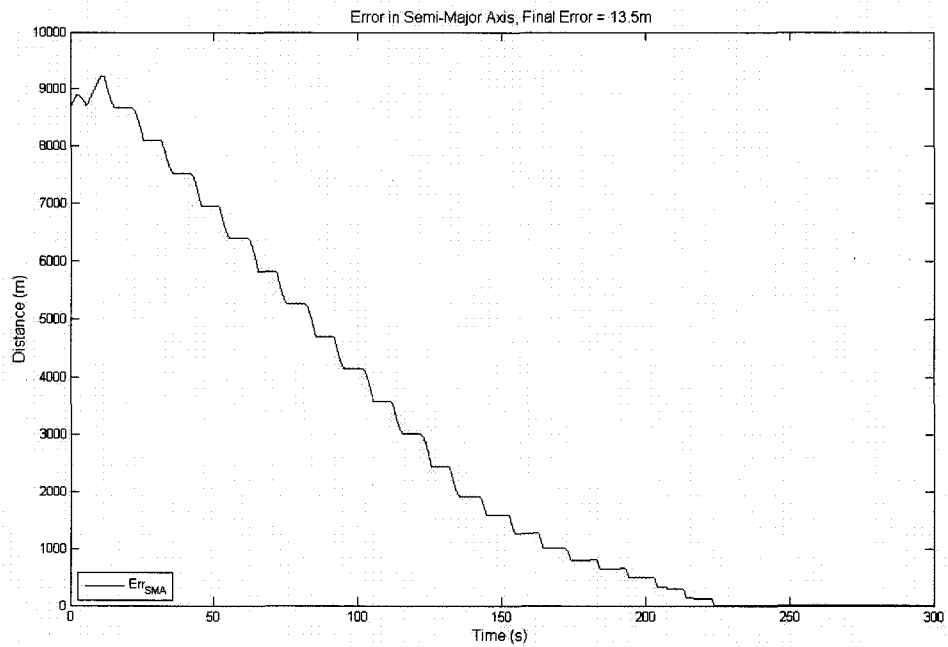


Figure 5-11: SMA error for the nutation case with relays

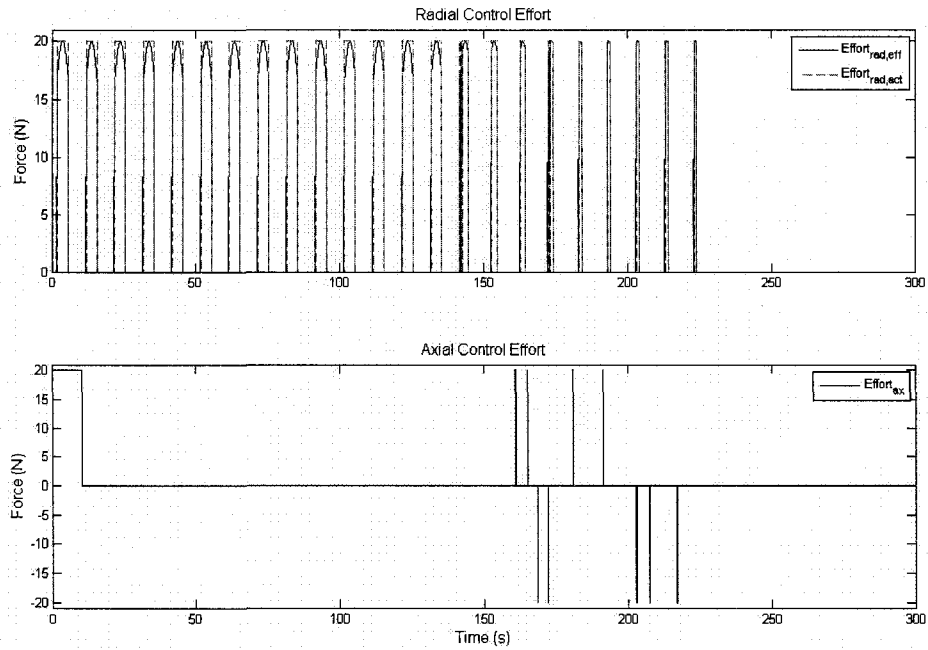


Figure 5-12: Thrust profile for the nutation case with relays

5.4 Study Four: Thruster Bias Only

The last disturbance to account for is thruster bias, which allows for the possibility that the thrusters are firing either “hot” or “cold,” i.e. they are firing more or less than expected. The disturbance assumed here is a simplistic case where all radial and axial thrusters are firing cold at 95% of nominal force F_T . Figure 5-13 shows the errors and ΔV used for this scenario. Table 5.5 lists the results. Again, all errors and efficiencies are within desired values. The most noticeable deviation from the ideal case is the time that the system takes to correct errors, since there is less force available. However this does not cause any increases in errors, which would be expected if the system is assumed to have instant knowledge of its state vector and therefore is capable of recognizing the loss of available force.

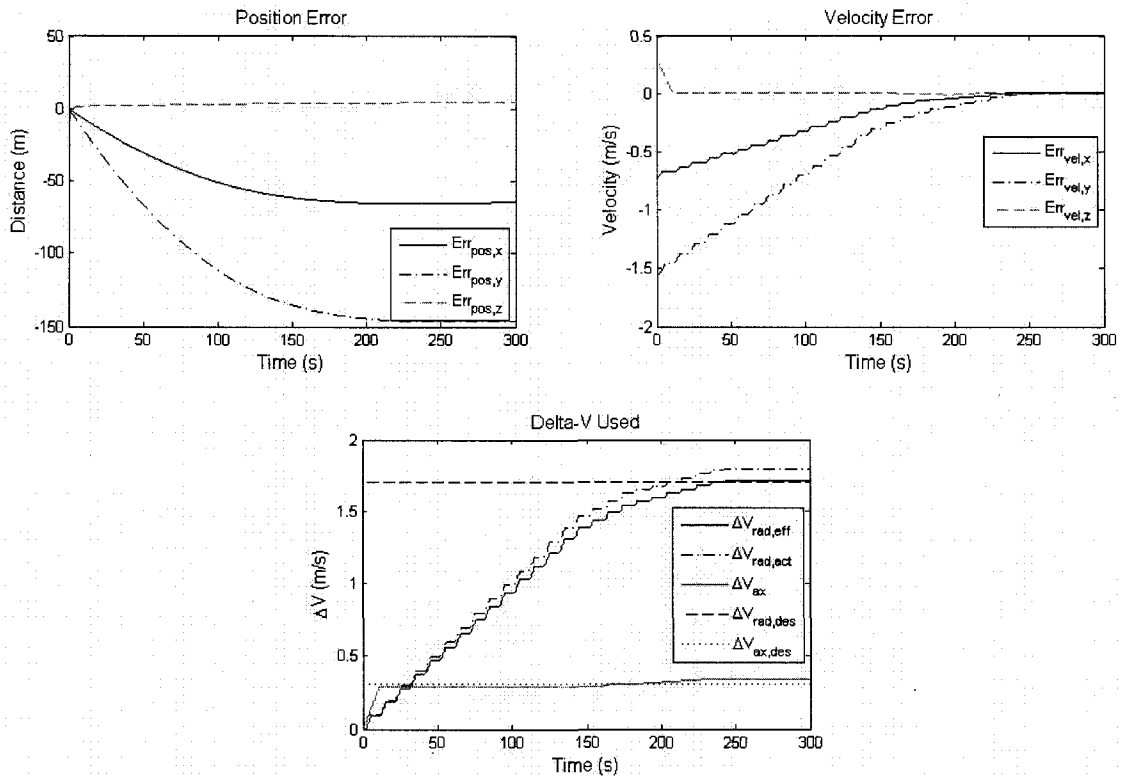


Figure 5-13: Position error, velocity error and ΔV used for the thruster bias case

THRUSTER BIAS	
Simulation Results:	
Original SMA Error:	8667.2m
Final SMA Error:	49.9m
Fuel Efficiency:	
Radial:	94.84%
Axial:	89%
Total:	94.64%
Resultant Velocity Error:	0.87%

Table 5.5: Results from the thruster bias case

Figure 5-14 shows the SMA error over the course of the maneuver. Figure 5-15 shows the control effort for the radial and axial thrusters. Note that the bias is visible in both thrust profiles.

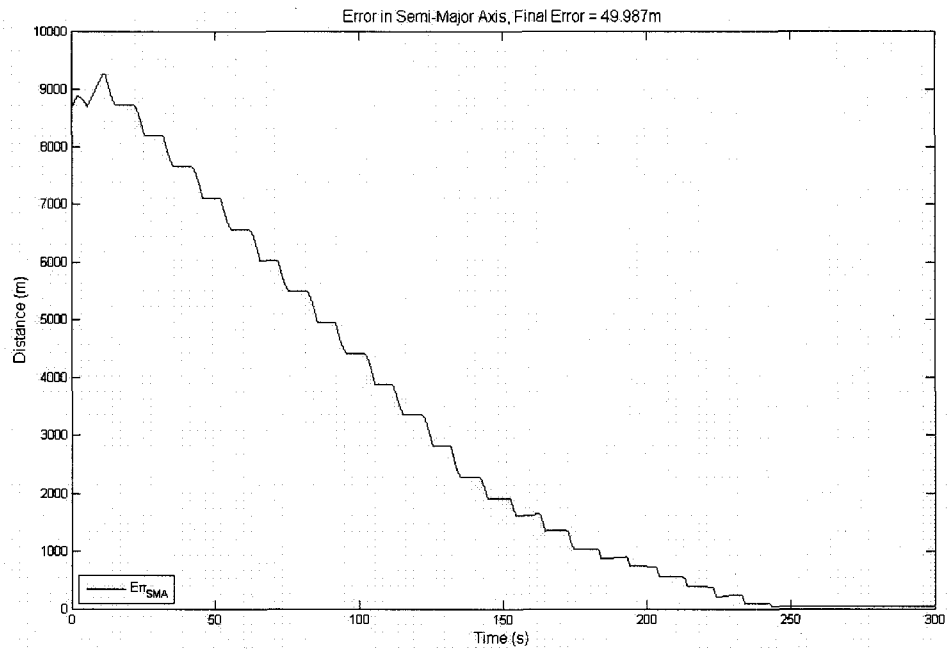


Figure 5-14: SMA error for the thruster bias case

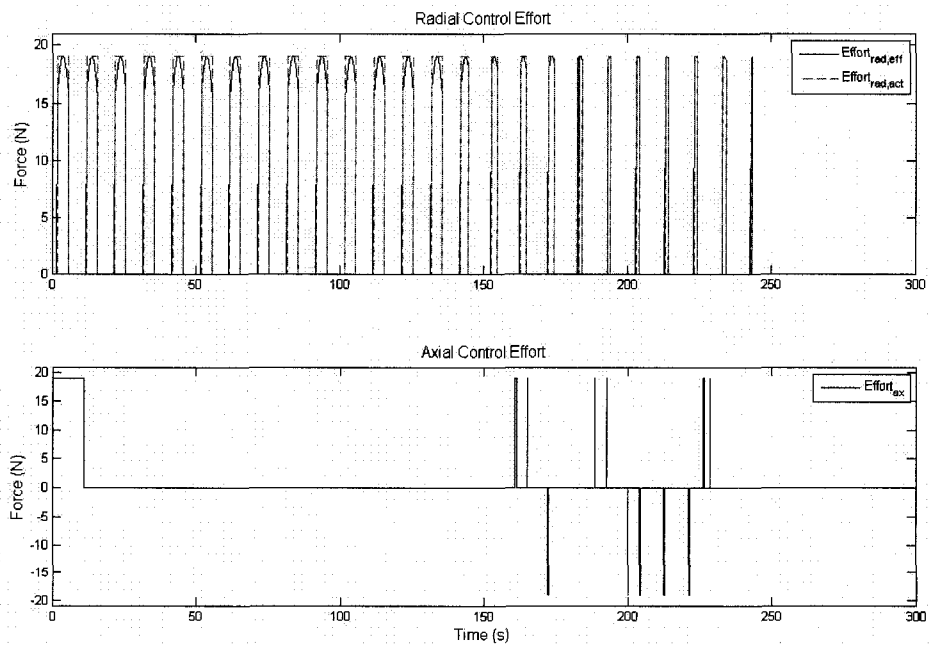


Figure 5-15: Thrust profile for the thruster bias case

5.5 Study Five: Nutation, Misalignments and Thruster Bias

The following results include all of the previous disturbances in this research (referred to as the worst case scenario). From this point on, unless otherwise stated, all results are from simulations which include nutation and thruster biases and misalignments. Figure 5-16 shows the position error, velocity error and ΔV used for this worst case scenario and Table 5.6 lists the results. Again, even with all disturbances included, the efficiency and errors are within desired thresholds. The success of the controller despite disturbances is likely due to the timing and manipulation of the control signal before it is sent to the thruster model. Because of the axial delay and the relays with hysteresis, much of the fluctuating errors, whether due to noise, nutation, or misalignments, are ignored.

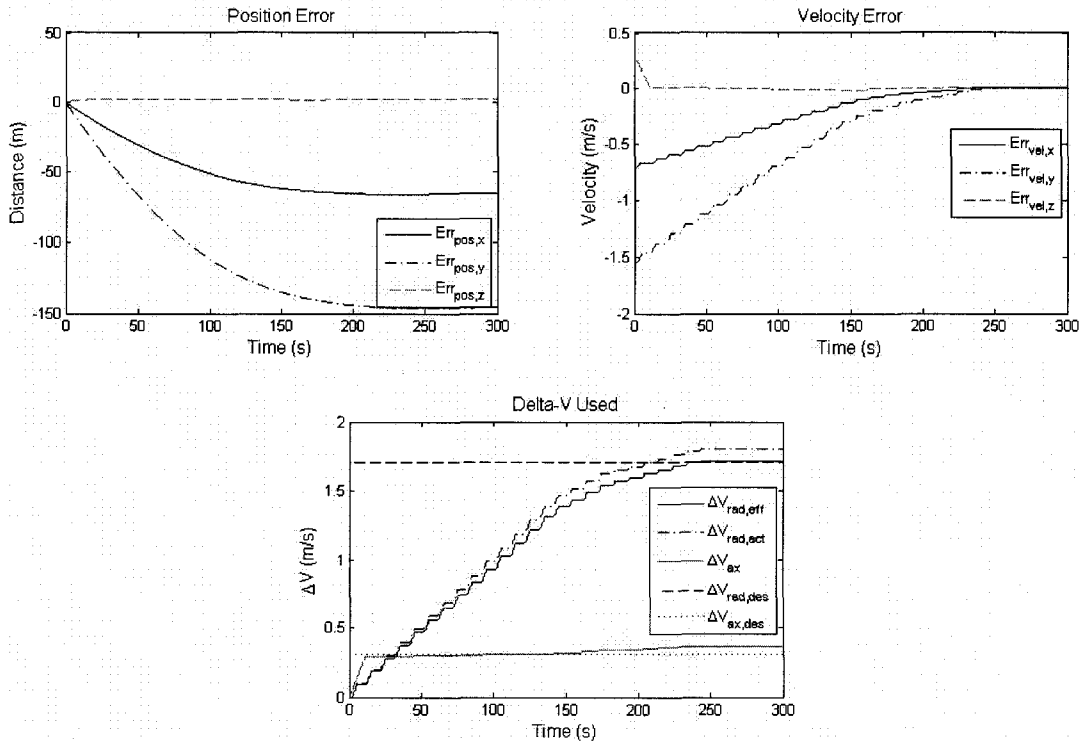


Figure 5-16: Position error, velocity error and ΔV used for a worst case scenario

WORST CASE	
Simulation Results:	
Original SMA Error:	8667.2m
Final SMA Error:	49.9m
Fuel Efficiency:	
Radial:	94.75%
Axial:	83.58%
Total:	94.33%
Resultant Velocity Error:	0.93%

Table 5.6: Results for a worst case scenario

Figure 5-17 shows the SMA error over the course of this maneuver. Figure 5-18 shows the radial and axial thrust profiles, on which can be seen the effects of the thruster misalignment and bias.

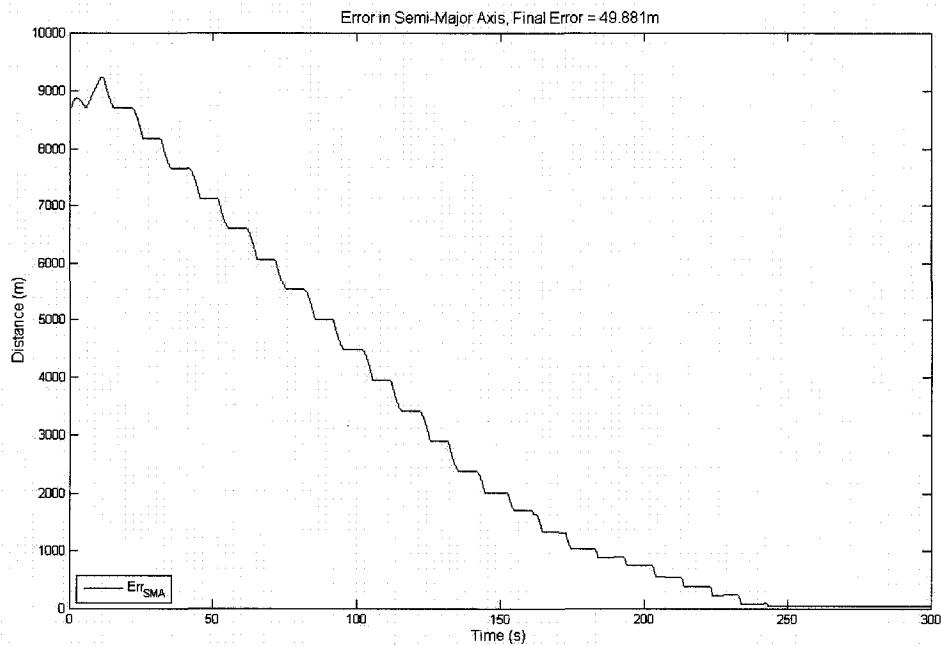


Figure 5-17: SMA error for a worst case scenario

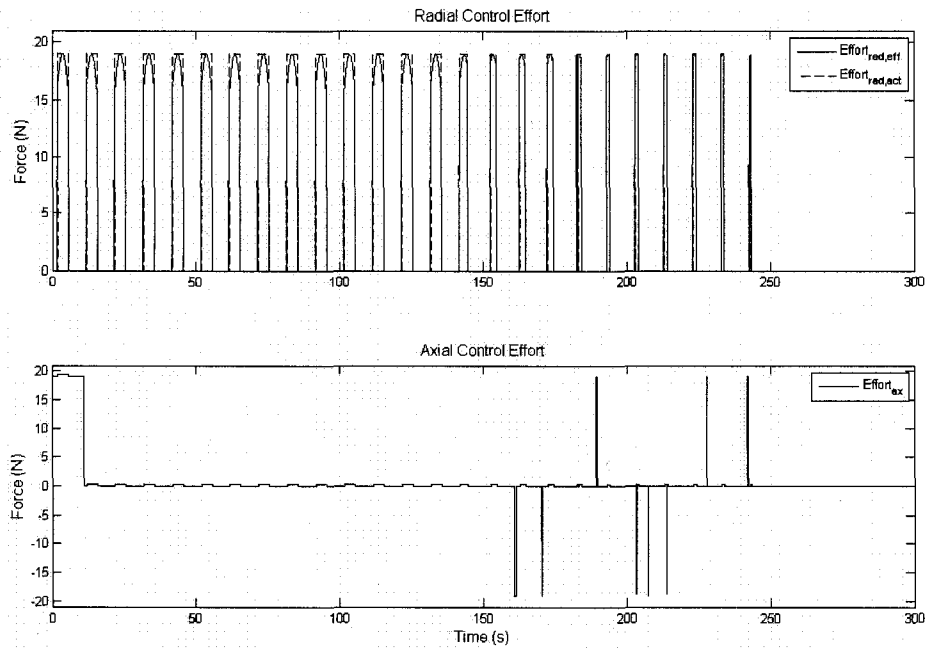


Figure 5-18: Thrust profile for a worst case scenario

Again, the previous tests have all been performed for only one spacecraft orientation. The possibility of sensitivity to initial orientations must be considered. The following section investigates this possibility.

5.6 Sensitivity to Orientation

It is highly improbable that mission design engineers will be able to predict the spacecraft orientation at the time that an orbit transfer must take place. At best, it is possible to give a maximum axial tilt with reference to the inertial z-direction, leaving the remaining two rotations uncertain. Thus it is necessary that any autonomous orbit transfer control be insensitive to changes in orientation, to within this specified maximum deviation from the inertial z-axis. In order to test this, the normal simulation was run

through embedded loops using MATLAB in which the Euler angles, described in section 2.3, were changed iteratively. The inner loop changes the axial tilt, or θ , from -10° to 10° in increments of 2° . After each case in which $\theta = 10^\circ$, the outer loop resets θ to -10° and increments the first Euler angle, ψ , by $\pi/10$ radians or 18° and begins incrementing θ anew. There are 100 unique axial alignments that are tested by this method and all alignments are coupled with the associated ΔV error for that case. The data from this test is output visually and numerically; the visual output is in the form of a three-dimensional plot in which all tested axial tilts are shown in reference to the inertial frame.

Figure 5-19 shows the three-dimensional image of results and Figure 5-20 shows this image from top-down. In Figure 5-20 the data points are plotted as shapes, where each shape represents a level of ΔV error, so as to try to determine any patterns of relative success or failure. The bar graph in Figure 5-21 shows the occurrence of a range of ΔV error for this case. The data from this test reveals that there is one failed case (ΔV error equal to 1.01%). Though it is not easily seen on the figure of data points, this failed case belongs to the body orientation of $\psi = 36^\circ$ and $\theta = 0^\circ$. What is interesting to note is that all points depicted on Figure 5-20 represent unique orientations with the exception of $\theta = 0^\circ$ (no axial tilt); each simulation loop runs through the zero-tilt orientation. Thus there are ten different cases where there is no axial tilt. The only difference between these points is the initial facing direction of the spacecraft, φ (if there is no axial tilt, ψ and φ are equivalent rotations). This indicates that not only is the controller sensitive to the initial orientation of the body frame, but also to the initial facing direction of the satellite—or from the perspective of the body frame, it is sensitive to the initial direction of the error vector.

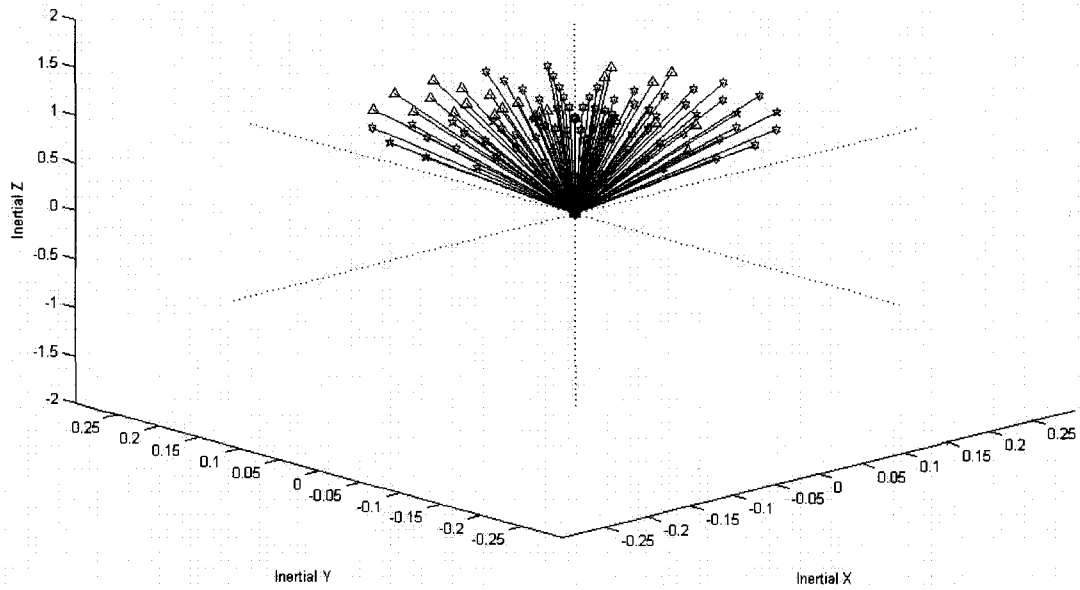


Figure 5-19: Three-dimensional visual results from the tilt test, depicting all 100 unique axial tilts with respect to the fixed inertial frame (dotted lines).

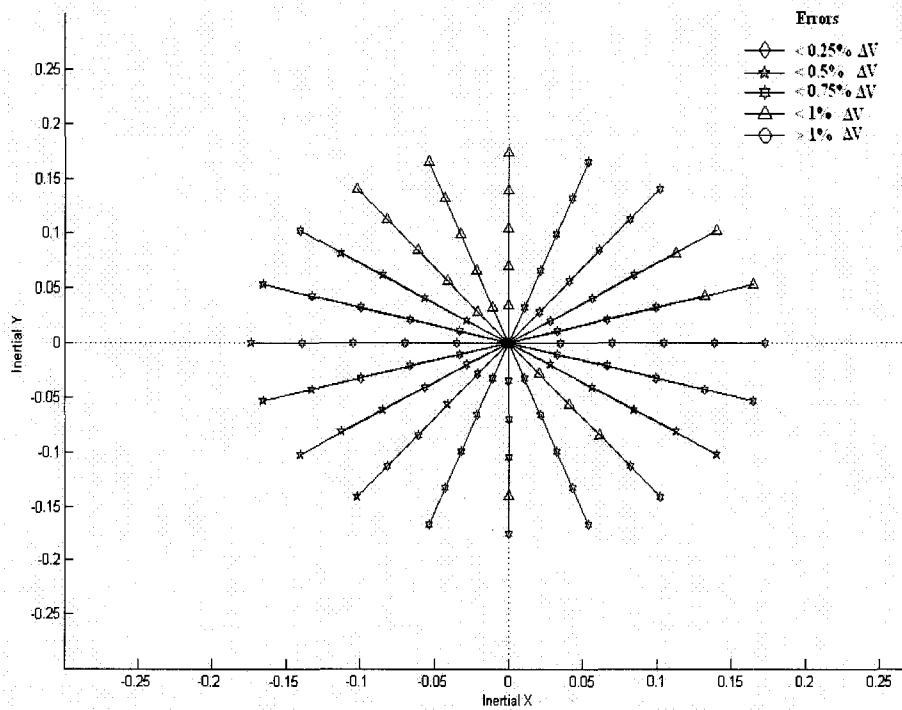


Figure 5-20: Top-down image of results from the tilt test, $\phi = 0^\circ$

Distribution of Delta-V Error Percentages, $\phi = 0$

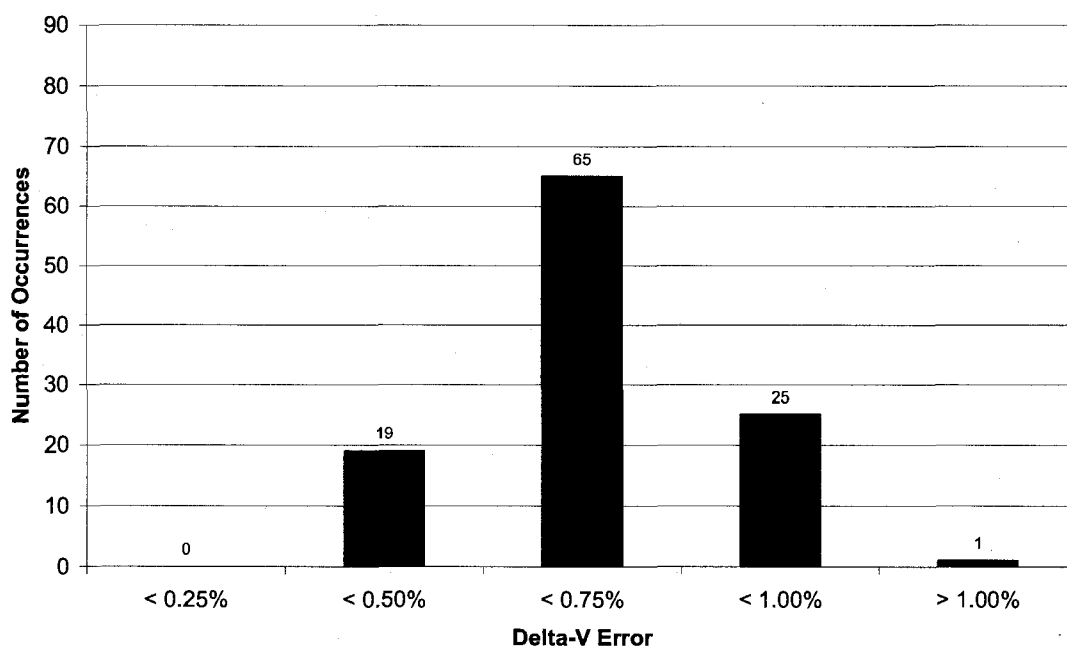


Figure 5-21: Number of occurrences of ΔV error ranges, $\phi = 0^\circ$

To qualify the controller's sensitivity to the satellite's initial facing direction, ϕ is rotated by 180° and the simulation is rerun. Figure 5-22 shows the visual output from this rotated scenario and the number of occurrences of ΔV error ranges is depicted in the bar graph of Figure 5-23. Here, the controller is shown to have a 100% success rate for meeting both SMA and ΔV criteria. Table 5.7 shows the overall results from both the $\phi = 0^\circ$ and $\phi = 180^\circ$ studies. Also note that in all tested cases, the total efficiency of the orbital maneuvers were at least 93% efficient.

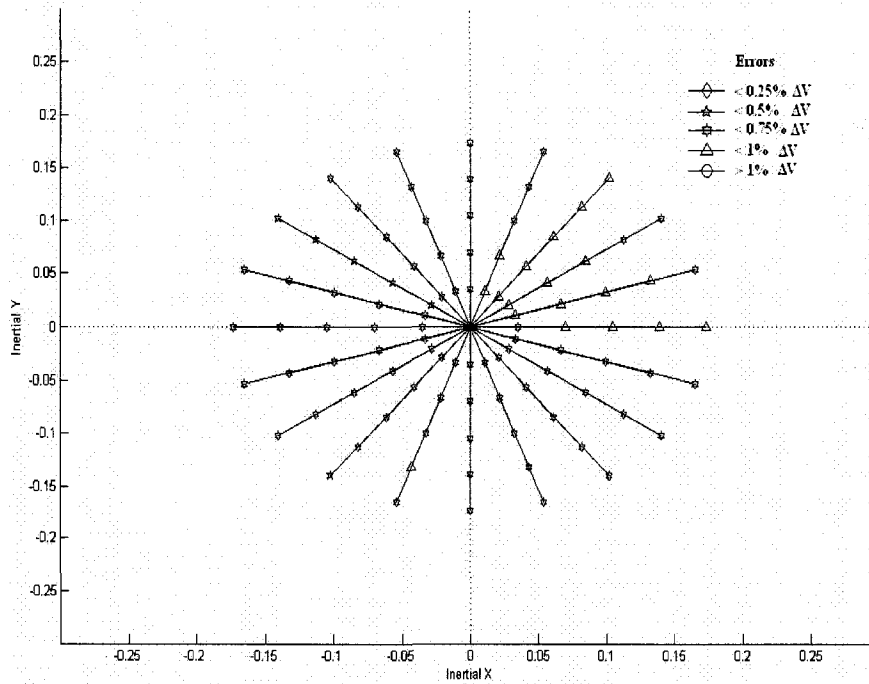


Figure 5-22: Top-down image of results from the tilt test, $\phi = 180^\circ$

Distribution of Delta-V Error Percentages, $\phi = 180$

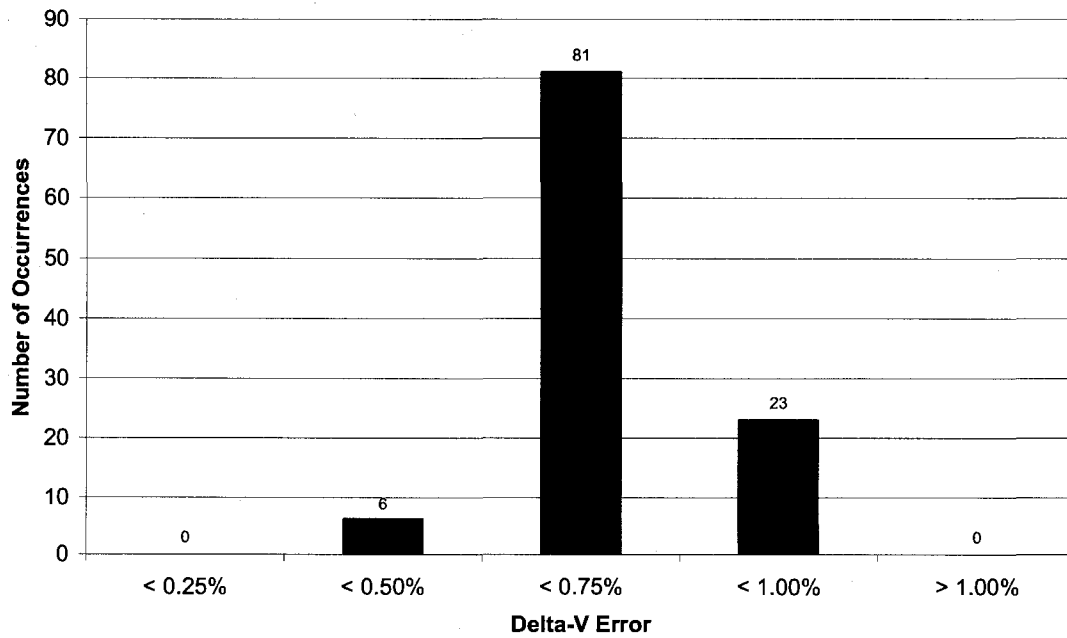


Figure 5-23: Number of occurrences of ΔV error ranges, $\phi = 180^\circ$

Tilt Test Results		
	$\varphi = 0^\circ$	$\varphi = 180^\circ$
Max SMA err	49.991m	49.998m
Min SMA err	-11.021m	-15.384m
Avg SMA err	26.617m	38.238m
Max $ \Delta V $ err	1.01%	0.98%
Min $ \Delta V $ err	0.28%	0.28%
Avg $ \Delta V $ err	0.63%	0.66%

Table 5.7: Overall results from axial tilt test for $\varphi = 0^\circ$ and $\varphi = 180^\circ$

5.7 Use of Semi-Major Axis Shutoff vs. Delta-V Shutoff

As stated, it is possible that only one of the two success criteria will be measured and used as a shutoff. The following study examines the feasibility of using each criterion individually with regard to final error for both. For this study, eleven cases were used to test each shutoff condition's viability. In each case the Euler angle $\psi = 0^\circ$ and the axial tilt θ is incremented from -10° to 10° . Also, the PID gains listed in Table 4.1 were not changed for any of these studies. Table 5.8 lists the results when using only the SMA shutoff of ± 50 meters. For the orientations tested, using an SMA shutoff of 50 meters proves to be an accurate method of control, as all ΔV errors fall within the desired 1%. All tested cases were greater than 93% efficient in terms of projected to expended ΔV .

Next, the shutoff condition was changed to use a ΔV error within $\pm 1\%$. The results from this test are shown in Table 5.9. Of all of the eleven cases tested, only one case resulted in both tolerable ΔV and SMA errors. This would seem to indicate that the tighter of the two criteria is the SMA error; if the SMA error is met, there's more likelihood that the velocity error will also be close to zero. Here, all tested cases were greater than 94% efficient.

SMA Shutoff = 50m			
Axial Tilt [deg]	SMA error [m]	ΔV error	Efficiency
-10	49.45	0.80%	94.34%
-8	49.90	0.81%	94.06%
-6	49.86	0.84%	93.88%
-4	49.87	0.91%	93.79%
-2	49.81	0.99%	93.74%
0	49.87	0.85%	93.86%
2	49.43	0.71%	93.90%
4	49.88	0.60%	94.07%
6	49.93	0.56%	93.84%
8	49.99	0.88%	93.90%
10	49.90	0.70%	94.07%
Average	49.81	0.79%	93.95%

Table 5.8: Resulting errors and efficiencies when using an SMA shutoff of ± 50 meters

ΔV Shutoff = 1%			
Axial Tilt [deg]	SMA error [m]	ΔV error	Efficiency
-10	58.50	0.95%	94.94%
-8	61.85	0.93%	94.63%
-6	79.90	0.81%	94.42%
-4	75.82	0.93%	94.37%
-2	83.34	0.96%	94.29%
0	88.25	0.76%	94.41%
2	81.93	0.65%	94.45%
4	81.69	0.63%	94.36%
6	85.84	0.68%	94.25%
8	68.09	0.86%	94.63%
10	47.13	0.71%	94.42%
Average	73.85	0.81%	94.47%

Table 5.9: Resulting errors and efficiencies when using a ΔV shutoff of $\pm 1\%$

Lastly, all monitored shutoffs were removed from the system and the controller performance was re-evaluated. The results from this test are listed in Table 5.10. From the eleven cases tested in this study, only one failed to meet both success criteria. With the chosen gains from Table 4.1, it seems that this control is relatively successful in meeting both error criteria without having to monitor them in real time and is slightly less efficient than the cases using shutoffs, with all tested cases being at least 92% efficient.

No Controller Shutoffs			
Axial Tilt [deg]	SMA error [m]	ΔV error	Efficiency
-10	31.97	0.89%	94.32%
-8	32.53	0.90%	94.00%
-6	33.05	0.93%	93.68%
-4	32.77	0.98%	93.47%
-2	27.20	1.10%	92.82%
0	33.31	0.95%	93.62%
2	33.76	0.77%	93.97%
4	23.23	0.70%	93.92%
6	21.67	0.83%	93.65%
8	36.13	0.84%	93.33%
10	22.25	0.67%	93.74%
Average	29.81	0.87%	93.68%

Table 5.10: Resulting errors and efficiencies when using no controller shutoffs

5.8 Effect of Accelerometer Bias on Errors

The last study presented in this thesis is aimed at showing the effect of accelerometer bias on the controller. Until this point, no bias has been included in the accelerometer model. Most likely, any accelerometers used in the MMS mission will have an inherent bias of a few μg (micro-g, where $1\mu\text{g} = 9.81 \times 10^{-6} \text{ m/s}^2$). As the final accelerometer bias is as yet unknown, it was seen as valuable to test the effects of a range of biases on the control results. Table 5.11 lists the final SMA and ΔV errors versus the bias included in the system. From these results, it can be concluded that even small levels of bias ($>2\mu\text{g}$) could potentially ruin the effectiveness of the controller.

For bias levels greater than $2\mu\text{g}$, there is a sharp rise in ΔV error. It is believed that because certain levels of errors are ignored, due in part to the relay blocks described in Section 4.4.5, the system does respond to the effects of this bias, which generally scale the measured errors. Inevitably, after a certain level of accelerometer bias, the drift due

to integration of the signal heightens the errors to an unacceptable level. This is a major cause for concern when considering the feasibility of autonomous orbital control using limited sensors.

Bias Test Results		
Bias Level [μg]	SMA Error [m]	ΔV Error [m/s]
1	49.41	0.94%
2	46.51	1.01%
3	-1.67	1.48%
4	-35.84	1.67%
5	-112.14	2.14%
6	-221.21	2.91%
7	-250.94	3.21%
8	-288.08	3.45%
9	-313.51	3.75%
10	-350.67	4.02%

Table 5.11: Effect of accelerometer bias levels on the SMA and ΔV errors

CHAPTER 6

CONCLUSIONS AND FUTURE WORK

6.1 Research Summary

This thesis has presented the research performed in creating a closed-loop control for orbital maneuvers of the Magnetospheric MultiScale spacecraft. Before any definitive conclusions can be made about the results from the controller, it is vital to ensure that the system itself has a high level of fidelity to the true environment of the satellite; this includes obtaining accurate levels of sensor noise, actuator timing, nutation, real-time coordinate transformations, etc. It cannot be stressed enough that these numerous factors are often the difference between acceptable results and unacceptable results. Since the actual satellite cannot truly be tested in any accurate simulation of space, it is mission-critical that these factors be considered in all computer simulations beforehand. Given this, the results obtained from this simulation indicate a strong possibility of using closed-loop control for orbital transfers. Overall, with the inclusion of nutation, misalignments, thruster bias levels, satellite reorientation and sensor noise, the results from the linear controller were successful in over 99% of all tested cases when using a double-success shutoff in the system. However, with the controller design presented in this thesis, there are certain problem areas that arise when subjecting the controller to a variety of situations. The main problem of orientation sensitivity is believed to arise due to small

fluctuations in the error values which cause the errors to either extend beyond the relay threshold—and thus become controlled—or remain at the cusp of that threshold, undetected by the controller and adding significantly to the errors. When deciding upon the level of hysteresis in the relay, it is necessary to balance the benefit of ignoring perceived errors due to nutation and the problem of ignoring actual, inertial errors. This balance seems to have been struck to a certain degree by using the PID gains listed in Table 4.1.

There is ongoing discussion as to whether the error in semi-major axis between two orbits should be considered as a criterion for success. Part of the reason is that, as stated, the relationship between the SMA error and inertial (i.e. position and velocity) errors is easily described when considering only in-track directions. In vector form, this relationship is harder to predict. From the results of these simulations, it seems that although actively monitoring and correcting the semi-major axis error should ensure a low velocity error, there is a large possibility that even finer velocity error resolution could be performed if the error in semi-major axis was neglected. For the purposes of this research, the PID gains and relay levels were not tuned to provide optimized velocity error resolution, but rather a combination of low velocity and SMA errors.

With respect to the fuel efficiency of the orbital maneuvers, in terms of projected ΔV to expended ΔV , all tested cases were at least 92% efficient. Using a double-shutoff method, all tested cases were at least 93% efficient. These efficiency values include the “wasted” ΔV from each radial thrust. With an initial burn angle window of $\pm 33^\circ$, radial burns will have a maximum efficiency of about 95%, and given a nominal 1° misalignment angle, an additional loss of 1.7% is expected (due to the necessary axial

corrections). This gives a total expected radial efficiency of about 93%. With this figure in mind, a minimum total efficiency of 92% seems credible and reasonable.

The result of including accelerometer bias into the system model is overall poor error resolution. When almost any level of bias is included in the accelerometer model, the results quickly degrade to the point of becoming unacceptable. Although no specifications regarding bias levels are known as of yet, it is beneficial to flight analysis engineers to be able to qualify the response of the system over a range of possibilities.

6.2 Future Work

The system presented in this thesis is relatively accurate, yet not fully complete. In order to truly gauge the potential for using autonomous orbit transfer control, it is vital that all details be accounted for. Also, it is important to fully qualify the behavior of results in as many situations as possible. Among the work remaining to be done are the following:

- Fully characterize the sensitivity of the orbital controller to initial orientation. In this thesis, over 200 unique scenarios were examined in an attempt to gauge the quality of all possible results. However, more scenarios need to be tested to complete this task, particularly in regard to the initial facing direction of the spacecraft for any given axial tilt.
- Include more sensor dynamics, in particular the characteristics of the star trackers. As yet no star tracker noise or bias levels have been included in this system. This step will ensure that all possible variables are taken into account with regard to the effect of noise levels on overall results.

- Include more accurate thruster layouts, allowing for the possibility of radial-radial or axial-axial misalignments and imbalances.
- Include discrete-time signals and zero-order holds to represent the delays in any commands from ground stations to the satellite, if relevant, since these commands are not actually instantaneous.
- Perform more analysis using various types of controllers, including nonlinear controllers, to determine if the results presented in this thesis are capable of being improved and at what cost to the processing time on board the spacecraft. Preliminary results using a simple sliding-mode controller suggest that, using this control scheme, there is little room for improvement due to actuator saturation. However, no definitive conclusions can be made without further development of other controller forms.
- Fully augment and integrate both this autonomous orbit controller and the autonomous attitude controllers presented in [1] and re-evaluate performance statistics. This combination of orbit and attitude control systems will ensure that the system is stable and controllable during all phases of orbit transfer.

BIBLIOGRAPHY

- [1] N. Mushaweh. An observer-based attitude and nutation control and flexible dynamic analysis for the NASA Magnetospheric MultiScale Mission. Master's thesis, University of New Hampshire, 2007.
- [2] K. Koprubasi. Spacecraft attitude and angular rate estimation using sliding mode observers. Master's thesis, University of New Hampshire, 2004.
- [3] D. Clemente. "Optimization of a tetrahedral satellite formation". *Journal of Spacecraft and Rockets*, 42:699-710, 2005.
- [4] J.R. Wertz (Ed.). *Spacecraft Attitude Determination and Control*. D. Reidel, Dordrecht, The Netherlands, 1978.
- [5] M.H. Kaplan. *Modern Spacecraft Dynamics and Control*. Wiley, New York, 1989.
- [6] T. Logsdon. *Orbital Mechanics: Theory and Applications*. Wiley, New York, 1998.
- [7] D.A. Vallado. *Fundamentals of Astrodynamics and Applications*. Microcosm Press, El Segundo, California, 2001.
- [8] B. Wei. *Space Vehicle Dynamics and Control*. American Institute of Aeronautics and Astronautics, Inc., 1998.
- [9] R.B. Noll et al. *Spacecraft Attitude Control During Thrusting Maneuvers*. National Aeronautic and Space Administration, Washington, D.C., 1971.

APPENDICES

APPENDIX A

MATLAB FILE

This appendix contains the MATLAB m-file `OrbCont1.m` which establishes all parameters, performs initial coordinate transformations and conversions, creates all necessary values, runs the main simulation and outputs all data into figures or as text.

```
% MMS ORBITAL CONTROLLER
% DOUBLE SHUTOFF OPTION, SPIN DYNAMICS INCLUDED, SET TO RADIAL/AXIAL
  OUTPUT
% M. BORRELLI
% LAST UPDATE: 4/24/08

clear
clc

% Given Parameters

M = 710;           % total mass of s/c [kg]
F_thrust = 20;    % N
mu_e = 3.986e5*10^9; % grav. constant of Earth [m^3/sec]
R_e = 6378136.3;  % radius of Earth [m]

% Initial Ephemeris

a = 42095.7*10^3; % semi-major axis [m]
e = 0.81818;     % eccentricity
i = .4898;       % orbital inclination
Omega = 0;       % ascending node
w = .2618;       % argument of perigee
Param = a*(1-e^2); % parameter [m]
theta = pi;      % true anomaly
r = Param/(1+e*cos(theta)); % position [m]

% Converted to Cartesian Position
x = r*(cos(w+theta)*cos(Omega) - cos(i)*sin(w+theta)*sin(Omega));
y = r*(cos(w+theta)*sin(Omega) + cos(i)*sin(w+theta)*cos(Omega));
z = r*(sin(w+theta)*sin(i));

% Initial Velocity
xdot = sqrt(mu_e/Param)*((cos(theta)+e)*(-sin(w)*cos(Omega) -
  cos(i)*sin(Omega)*cos(w)) - sin(theta)*(cos(w)*cos(Omega) -
  cos(i)*sin(Omega)*sin(w)));
```

```

ydot = sqrt(mu_e/Param)*((cos(theta)+e)*(-
    sin(w)*sin(Omega)+cos(i)*cos(w))-
    sin(theta)*(cos(w)*sin(Omega)+cos(i)*cos(Omega)*sin(w)));
zdot = sqrt(mu_e/Param)*((cos(theta)+e)*sin(i)*cos(w)-
    sin(theta)*sin(i)*sin(w));

V0 = [xdot;ydot;zdot];
X0 = [x;y;z];

% Unit Vector Creation
V0mag = sqrt(xdot^2+ydot^2+zdot^2);
V0u = [xdot/V0mag;ydot/V0mag;zdot/V0mag];

% Inertial Frame Coordinate Vectors
X_old = [1;0;0];
Y_old = [0;1;0];
Z_old = [0;0;1];

% Establish Orbit-Defined Coordinate System
X_new = V0u;
Z_new = [0;-sin(i);cos(i)];
Y_new = cross(X_new,Z_new);

% Delta V vector transformation into Inertial Frame
dVmag = 1; % m/s
dV_old = [dVmag;dVmag;dVmag];
transf = [X_new(1) X_new(2) X_new(3);...
Y_new(1) Y_new(2) Y_new(3);...
Z_new(1) Z_new(2) Z_new(3)];
dV = inv(transf)*dV_old;
dVdes = sqrt(dV(1)^2+dV(2)^2+dV(3)^2);

% Initial Radial Firing Window
FA0 = 33.3*pi/180; % rad

% Apply to V0
V = V0 + dV;
X = X0;

% Body Rates
nom_rate = pi/10; % rad/sec
omega_x = 1*.0111*nom_rate; % rad/sec
omega_y = 0*nom_rate; % rad/sec
omega_z = nom_rate; % rad/sec
b_rates = [omega_x;omega_y;omega_z];

% ----- INITIAL EULER ANGLES ----- %
Psi = 0*pi/180; % rad
Theta = -10e-9*pi/180; % rad
Phi = 0*pi; % rad

% Establish Initial Direction Cosine Matrix (3-1-3)
DCMi = [(cos(Phi)*cos(Psi)-sin(Phi)*cos(Theta)*sin(Psi))...
(cos(Phi)*sin(Psi)+sin(Phi)*cos(Theta)*cos(Psi))...
(sin(Phi)*sin(Theta));...

```

```

(-sin(Phi)*cos(Psi)-cos(Phi)*cos(Theta)*sin(Psi))...
(-sin(Phi)*sin(Psi)+cos(Phi)*cos(Theta)*cos(Psi))...
(cos(Phi)*sin(Theta));...
(sin(Theta)*sin(Psi))...
(-sin(Theta)*cos(Psi))...
(cos(Theta));

% Initial Radial & Axial BODY Delta V
dVb = DCMi*dV;
dVrad0 = sqrt(dVb(1)^2+dVb(2)^2);
dVaxi0 = abs(dVb(3));
dV0 = norm([dV(1) dV(2) dV(3)]);

% Inertial Frame & Initial Body Frame Visualization (not plotted)
n = 0:1;

x1=n*X_old(1);
x2=n*X_old(2);
x3=n*X_old(3);
y1=n*Y_old(1);
y2=n*Y_old(2);
y3=n*Y_old(3);
z1=n*Z_old(1);
z2=n*Z_old(2);
z3=n*Z_old(3);

x7=n*dV(1)/norm(dV);
y7=n*dV(2)/norm(dV);
z7=n*dV(3)/norm(dV);

% Flags for Sin/Cos Components of Radial Thrust
cos_flag = 1;
sin_flag = 1;

% Thruster Bias Percentages & Misalignment Degrees
RAMisalign = 1; % degrees
RAbias = 0.95;
if RAMisalign ~= 0 && RAbias ~= 0
RAMis = sind(RAMisalign);
T_limit_rad = RAbias;
T_limit_ax = RAbias;
elseif RAMisalign ~= 0
RAMis = sind(RAMisalign);
T_limit_rad = cosd(RAMisalign);
T_limit_ax = 1;
elseif RAbias ~= 0
RAMis = 0;
T_limit_rad = RAbias;
T_limit_ax = RAbias;
elseif RAMisalign == 0 && RAbias == 0
RAMis = 0;
T_limit_rad = 1;
T_limit_ax = 1;

end

```

```

% Accelerometer Bias + Noise
bias = 0*9.81e-6;    %m/s^2
noise_power = 1e-6;

%%%%%%%%%%%%%%%%%%%%%%%%%%%%%%%%%%%%%%%%%%%%%%%%%%%%%%%%%%%%%%%%%%%%%%%%
% Dean's Model Inputs
noise_freq = 100;

wf = 200 * 2*pi;

% Parameters of the Noise model
P_low = 7^2/(10-0)/2;% (sigma-rms)^2 / (2*bandwidth)
P_med = 70^2/(200-10)/2;% (sigma-rms)^2 / (2*bandwidth)
P_high = 1500^2/(10000-500)/2;% (sigma-rms)^2 / (2*bandwidth)
noise_seed = 2231;
w1 = 10 * 2*pi;
w2 = 10 * 2*pi;
w3 = 200 * 2*pi;
w4 = 200 * 2*pi;
w5 = 10000 * 2*pi;

%%%%%%%%%%%%%%%%%%%%%%%%%%%%%%%%%%%%%%%%%%%%%%%%%%%%%%%%%%%%%%%%%%%%%%%%

% CONTROLLER GAINS

P1coef = .5*0.3;    %Position P Gain
P2coef = 20*500;    %Velocity P Gain
I1coef = 0;        %Position I Gain
I2coef = 0*0.03;   %Velocity I Gain
D1coef = 0*20/6;   %Position D Gain
D2coef = 0;        %Velocity D Gain

P1 = P1coef*[1 0;0 1];
P2 = P2coef*[1 0;0 1];
P = [P1 P2];
I1 = I1coef*[1 0;0 1];
I2 = I2coef*[1 0;0 1];
I = [I1 I2];
D1 = D1coef*[1 0;0 1];
D2 = D2coef*[1 0;0 1];
D = [D1 D2];

%----- SLIDING MODE PARAMETERS ----- %
K1 = 1;
K2 = 10;
lambda1 = 1;
lambda2 = 1000;

% ----- PARAMETERS ----- %
% Axial Firing Delay + Pause
ax_delay = 00;    % sec
ax_dur = ax_delay + (dVaxi0)/(F_thrust/M);    % sec
ax_restart = ax_dur + 150;    % sec

```

```

% RELAY VALUES
rad_relay = 10;
ax_relay = 30;

% Controller Shutoff Criteria
burn_time = 300; % sec
sma_cutoff(1) = 50.0*dVmag; % m

% Simulation Parameters
maxtime = 1e-2; %Max time step
mintime = 1e-5; %Min time step
reltol = 1e-5; %Relative tolerance
abstol = 1e-6; %Absolute tolerance
runtime = 3e2;

% Run & Evaluate Simulation -----

%clc
disp(['Simulation ',int2str(count),' of ',int2str(num_sims)])

if sin_flag == 0 && cos_flag == 0
disp('-No sine or cosine radial thrust components considered')
elseif sin_flag == 0
disp('-Cosine component of radial thrust considered')
else
disp('-Both sine and cosine components of radial thrust considered')
end

if omega_x == 0 && omega_y == 0
disp('-No nutation rates included')
elseif omega_y == 0
disp(['-Nutation rate about x-axis = ',num2str(omega_x,2),'rad/s'])
elseif omega_x == 0
disp(['-Nutation rate about y-axis = ',num2str(omega_y,2),'rad/s'])
else
disp(['-Nutation rate about x-axis = ',num2str(omega_x,2),'rad/s'])
disp(['-Nutation rate about y-axis = ',num2str(omega_y,2),'rad/s'])
end

if RAMisalign == 0 && RAbias == 0
disp('-No radial or axial biases or misalignments')
elseif RAbias == 0
disp(['-Radial-Axial misalignment angle = ',num2str(RAmis*180/pi,2),'deg'])
elseif RAMisalign == 0
disp(['-Thruster bias = ',num2str(RAbias*100,2),'%'])
else
disp(['-Radial-Axial misalignment angle = ',num2str(RAmis*180/pi,2),'deg'])
disp(['-Thruster bias = ',num2str(RAbias*100,2),'%'])
end

```

```

if bias == 0
disp('-No Accelerometer bias included')
else
disp(['-Accelerometer bias = ',num2str(bias*1e6/9.81,2),'ug'])
end

sim('Orbit1')
l = length(xout);
t_burn = 0;

for count1 = 1:length(sma_err)
if abs(sma_err(count1)) > sma_cutoff
t_burn = t_burn + maxtime;
end

end

%-----%

figure

subplot(2,2,1), plot(time,pos_err(:,1),...
time,pos_err(:,2),'k-.',...
time,pos_err(:,3),'--')
title('Position Error','fontsize',12)
xlabel('Time (s)','fontsize',12)
ylabel('Distance (m)','fontsize',12)
legend('Err_{pos,x}','Err_{pos,y}','Err_{pos,z}','Location','Southeast'
)
hold on

subplot(2,2,2), plot(time,vel_err(:,1),time,vel_err(:,2),'k-
.',time,vel_err(:,3),'--')
title('Velocity Error','fontsize',12)
xlabel('Time (s)','fontsize',12)
ylabel('Velocity (m/s)','fontsize',12)
legend('Err_{vel,x}','Err_{vel,y}','Err_{vel,z}','Location','East')
hold on

subplot(2,2,3.5),
plot(time(1:length(DV)),DV(:,1),time(1:length(DV)),DV(:,2),'b-.',...
time(1:length(DV)),DV(:,3),'r',time(1:length(DV)),dVrad,'k--
',time(1:length(DV)),dVaxi,'k:')
title('Delta-V Used','fontsize',12)
xlabel('Time (s)','fontsize',12)
ylabel('\DeltaV (m/s)','fontsize',12)
legend('\DeltaV_{rad,eff}','\DeltaV_{rad,act}','\DeltaV_{ax}',...
'\DeltaV_{rad,des}','\DeltaV_{ax,des}','Location','East')
hold on

%-----%

```

```

figure

plot(time,sma_err,'k')
title(['Error in Semi-Major Axis, Final Error = ',...
num2str(sma_err(length(sma_err)),5),'m'],'fontsize',12)
xlabel('Time (s)','fontsize',12)
ylabel('Distance (m)','fontsize',12)
legend('Err_{SMA}','Location','SouthWest')

%-----%

figure

subplot(2,1,1), plot(time(1:length(ResEffort)),ResEffort(:,1),'k',...
time(1:length(ActEffort)),ActEffort,'k--')
title('Radial Control Effort','fontsize',12)
ylabel('Force (N)','fontsize',12)
legend('Effort_{rad,eff}','Effort_{rad,act}','Location','NorthEast')
axis([0 300 0 21])

subplot(2,1,2), plot(time(1:length(ResEffort)),ResEffort(:,2),'k')
title('Axial Control Effort','fontsize',12)
xlabel('Time (s)','fontsize',12)
ylabel('Force (N)','fontsize',12)
legend('Effort_{ax}','Location','NorthEast')
axis([0 300 -21 21])

disp('-----')
disp('Simulation Results:')

len = length(xout);
a_err = [sma_err(1),sma_err(len)];
fuel =
    [DVmag1(length(DVmag1),3),DVmag1(length(DVmag1),2),DVmag(length(DVmag1),1)];
disp(['-Original SMA Error: ',num2str(a_err(1),5),'m'])
disp(['-Final SMA Error: ',num2str(a_err(2),5),'m'])
disp(['-Fuel Efficiency is: (R) ',num2str(fuel(1),4),'%', '(A) ',...
num2str(fuel(2),4),'%', '(T) ',num2str(fuel(3),4),'%'])
err1 = norm(vel_err(length(vel_err),:));
err2 = norm(dV);
disp(['-Resultant Velocity Error: '...
num2str(err1,2),'m/s (', num2str(100*(err1/err2),3),'%')])

disp(' ')
disp(' ')

% Tilt Test Image

x_bf = DCMi*X_old;
y_bf = DCMi*Y_old;
z_bf = DCMi*Z_old;
x6 = n*x_bf(3);
y6 = n*y_bf(3);

```



```

z6 = n*z_bf(3);

figure(100)
plot3(2*x3,2*y3,2*z3,'kd:')
hold on
plot3(.4*x1,.4*y1,.4*z1,'kx:')
plot3(-.4*x1,-.4*y1,-.4*z1,'kx:')
plot3(.4*x2,.4*y2,.4*z2,'ko:')
plot3(-.4*x2,-.4*y2,-.4*z2,'ko:')
plot3(-2*x3,-2*y3,-2*z3,'kd:')

if abs(sma_err(length(sma_err))) < sma_cutoff &&
    norm(vel_err(length(vel_err),:)) < 0.01*.25*norm(dV0)
plot3(x6,y6,z6,'kd-')
elseif abs(sma_err(length(sma_err))) < sma_cutoff &&
    norm(vel_err(length(vel_err),:)) < 0.01*.5*norm(dV0)
plot3(x6,y6,z6,'kp-')
elseif abs(sma_err(length(sma_err))) < sma_cutoff &&
    norm(vel_err(length(vel_err),:)) < 0.01*.75*norm(dV0)
plot3(x6,y6,z6,'kh-')
elseif abs(sma_err(length(sma_err))) < sma_cutoff &&
    norm(vel_err(length(vel_err),:)) < .01*norm(dV0)
plot3(x6,y6,z6,'k^-')
else
plot3(x6,y6,z6,'ko-')

xlabel('Inertial X')
ylabel('Inertial Y')
zlabel('Inertial Z')
grid on
axis([-0.4 0.4 -0.4 0.4 -2 2])
end
toc

```

APPENDIX B

SIMULINK BLOCK DIAGRAMS

This appendix shows the main system, Orbit1.mdl, and all major subsystems which propagate and control the satellite model. Each system or subsystem is described briefly.

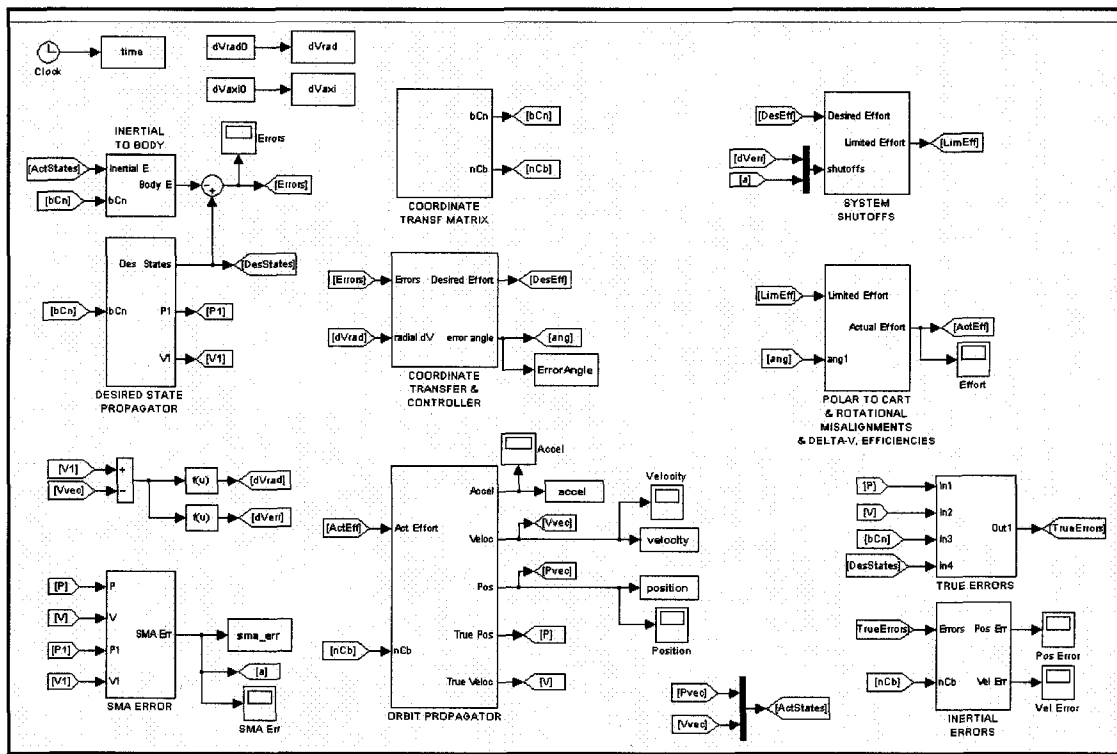


Figure B-1: Main system in Orbit1.mdl.

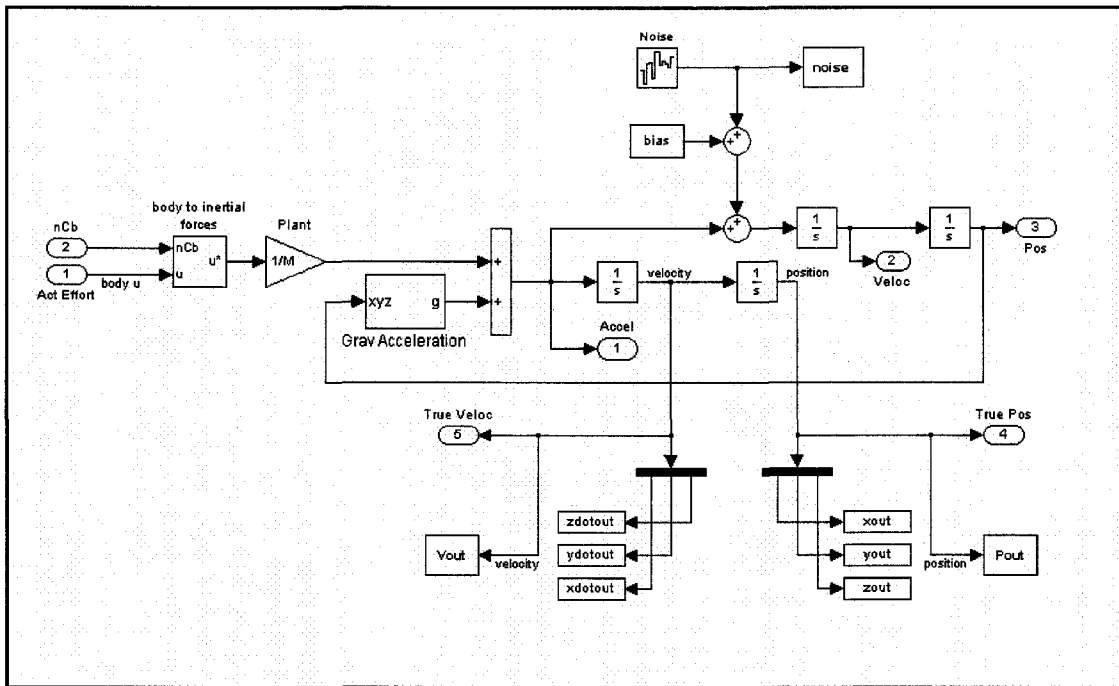


Figure B-2: True satellite model, including accelerometer model, gravitational acceleration and plant dynamics

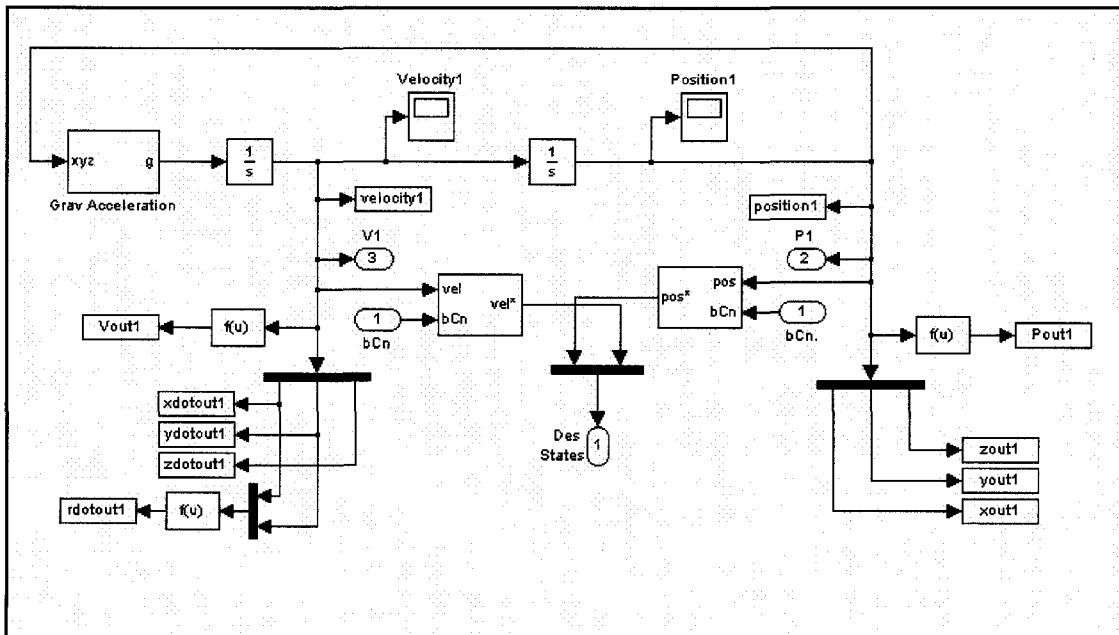


Figure B-3: Target satellite model, including gravitational acceleration, which outputs position and velocity vectors to generate and error vector

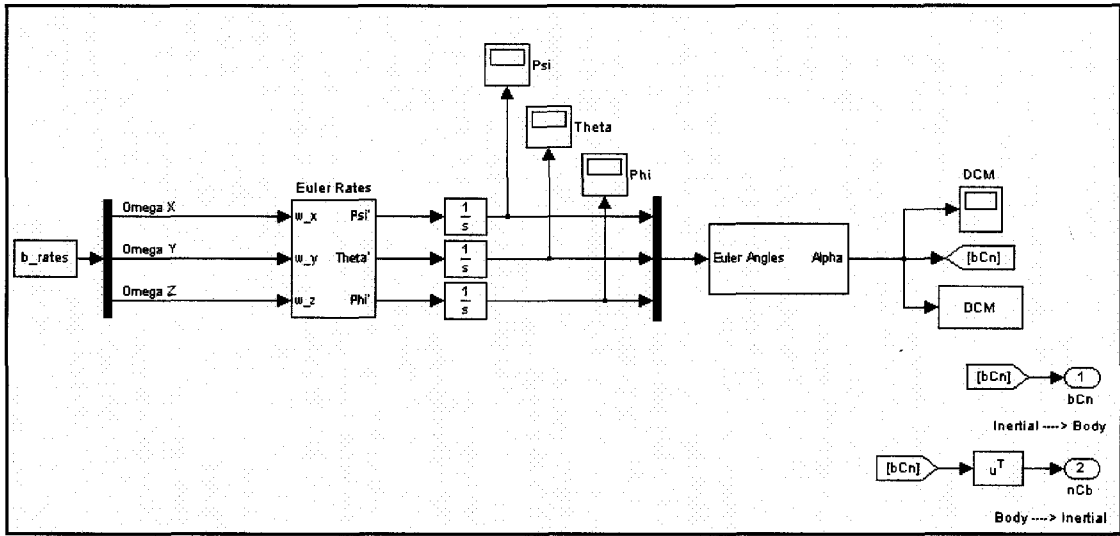


Figure B-4: Direction Cosine Matrix generator, including Euler Rate subsystem

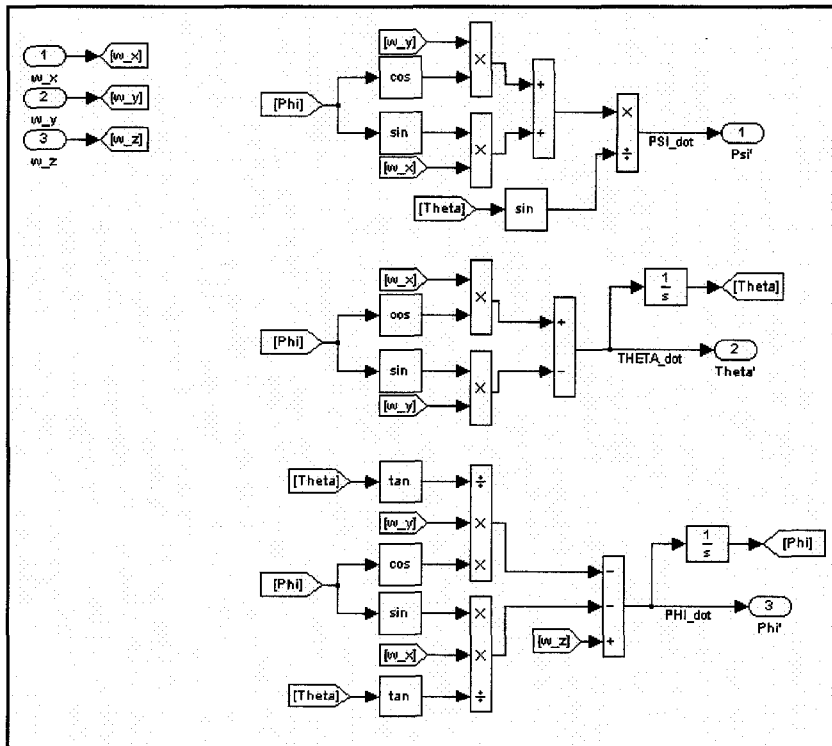


Figure B-5: Euler angle rate calculation based upon body rate inputs and Euler angle initial conditions

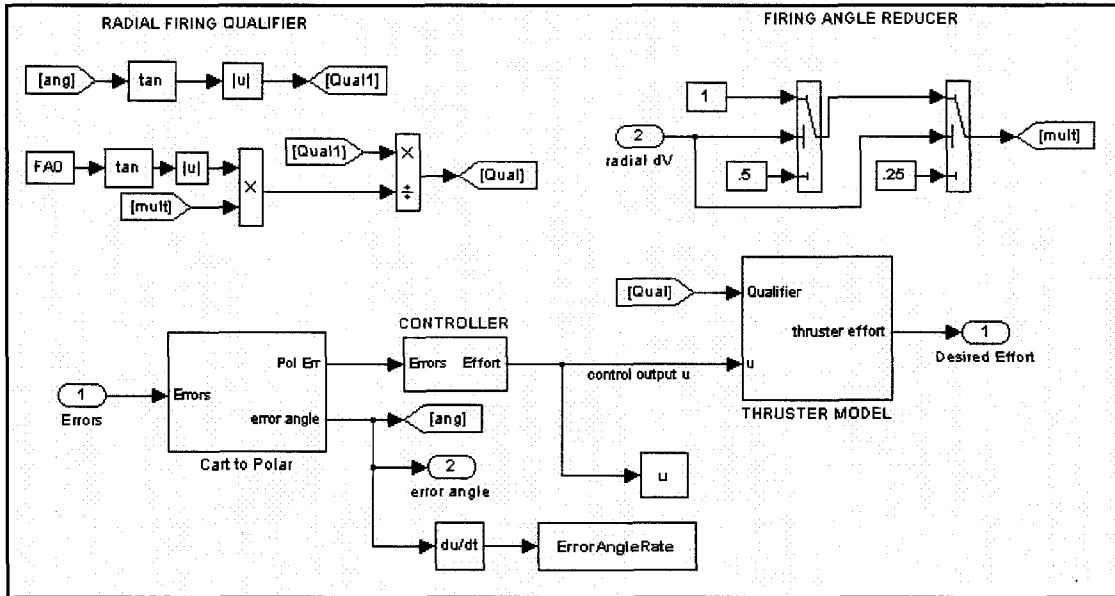


Figure B-6: Controller subsystem, including radial thruster timing algorithm and radial burn angle window reducing algorithm, as well as the thruster model

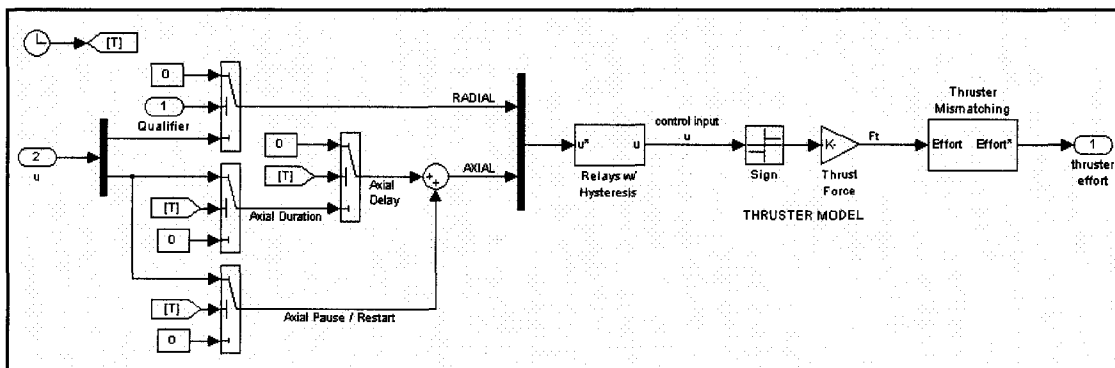


Figure B-7: Thruster model subsystem, including axial pause and relays, as well as the thruster misalignment/bias subsystem

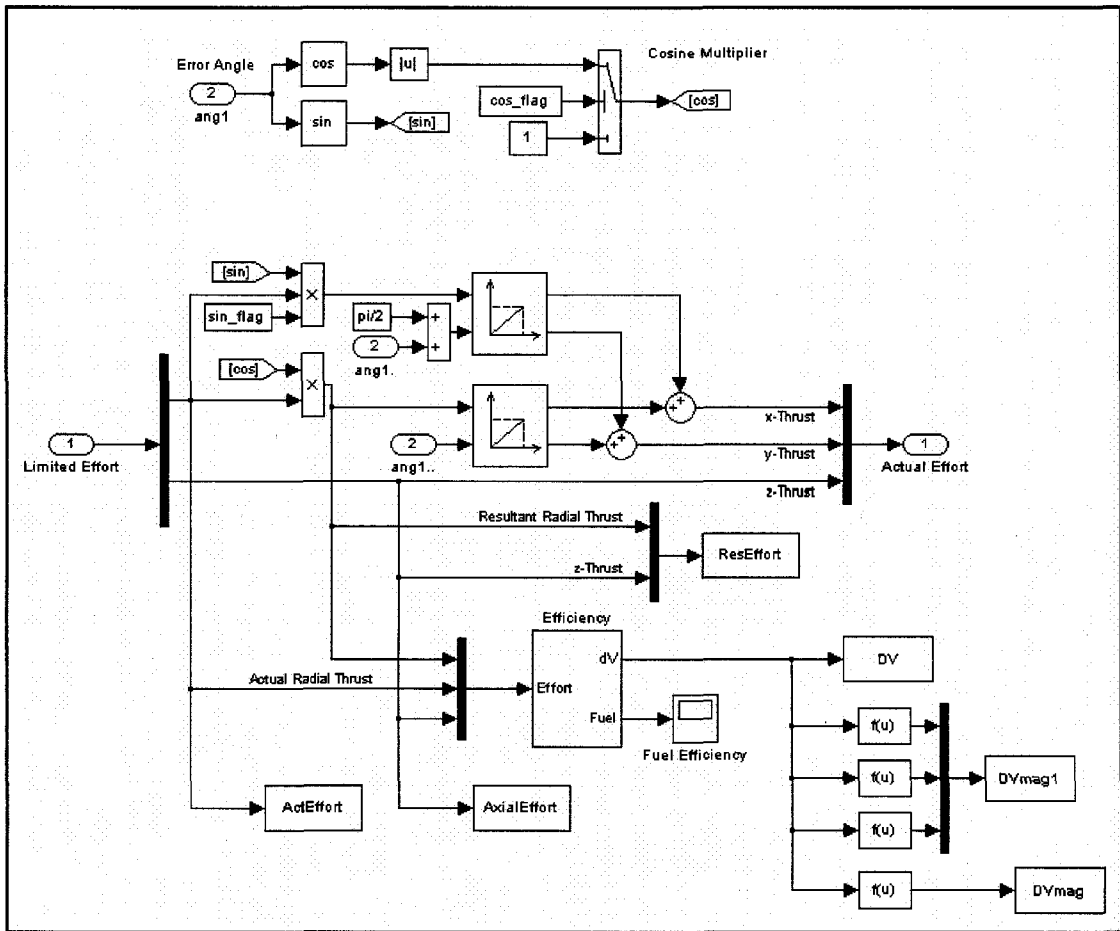


Figure B-8: Final thruster calculations, including sine/cosine components of radial force and the efficiency calculation and Delta-V subsystem

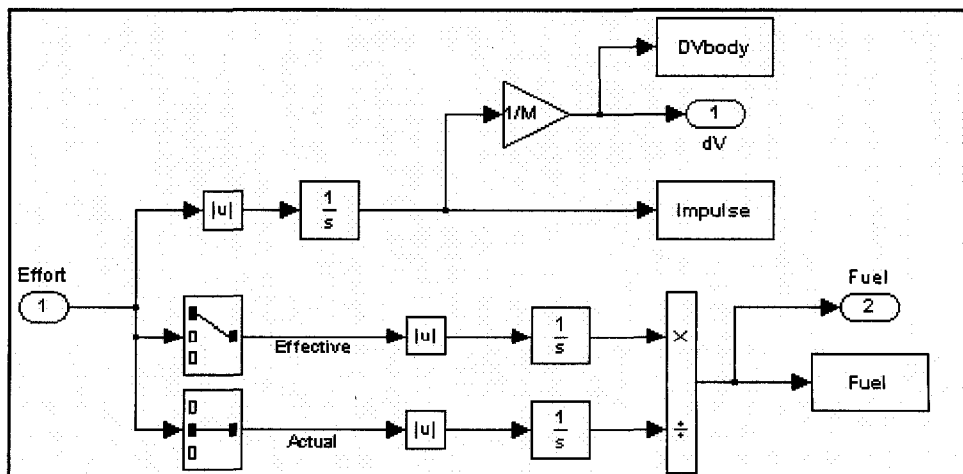


Figure B-9: Delta-V subsystem

APPENDIX C

SEMI-MAJOR AXIS SENSITIVITY DERIVATION

The following derivation was performed by Dean Tsai of NASA GSFC. This derivation shows the sensitivity of the change in an orbit's semi-major axis to the changes in the in-track (along-orbit) position and velocity. The ending relationship was used as a basis for the PID gains of the chosen controller and the gains were then tuned from these original values to optimize the results.

$$\text{Energy_Balance} : v^2 = \frac{2\mu}{r} - \frac{\mu}{SMA}$$

$$dSMA = \frac{\partial SMA}{\partial r} dr + \frac{\partial SMA}{\partial v} dv$$

$$dSMA = \frac{2\mu^2}{(v^2 r - 2\mu)^2} dr + \frac{2r^2 \mu v}{(v^2 r - 2\mu)^2} dv$$

$$\Delta SMA = (6.157 \times 10^{-1}) \Delta r + (9.115 \times 10^3) \Delta v$$